



1 **Light-absorbing black carbon and brown carbon components of smoke aerosol from**
2 **DSCOVER EPIC measurements over North America and Central Africa**

3

4 Myungje Choi^{1,2}, Alexei Lyapustin², Gregory L. Schuster³, Sujung Go^{1,2}, Yujie Wang^{1,2}, Sergey
5 Korkin^{1,2}, Ralph Kahn^{2,4}, Jeffrey S. Reid⁵, Edward J. Hyer⁵, Thomas F. Eck^{1,2}, Mian Chin², David
6 J. Diner⁶, Olga Kalashnikova⁶, Oleg Dubovik⁷, Jhoon Kim⁸, Hans Moosmüller⁹

7

8 ¹Goddard Earth Sciences Technology and Research (GESTAR) II, University of Maryland
9 Baltimore County, Baltimore, MD, USA

10 ²NASA Goddard Space Flight Center, Greenbelt, MD, USA

11 ³NASA Langley Research Center, Hampton, VA, USA

12 ⁴Laboratory for Atmospheric and Space Physics, The University of Colorado Boulder, Boulder,
13 CO, USA

14 ⁵US Naval Research Laboratory, Monterey, CA, USA

15 ⁶Jet Propulsion Laboratory, California Institute of Technology, Pasadena, CA, USA

16 ⁷Laboratoire d'Optique Atmosphérique, Université de Lille-1, CNRS, Villeneuve d'Ascq, France

17 ⁸Department of Atmospheric Sciences, Yonsei University, Seoul, Republic of Korea

18 ⁹Laboratory for Aerosol Science, Spectroscopy, and Optics, Desert Research Institute, Reno, NV,
19 USA

20

21 Correspondence to: Myungje Choi (myungje.choi@nasa.gov)

22



23 **Abstract**

24 Wildfires and agricultural burning generate seemingly increasing smoke aerosol emissions,
25 impacting societal and natural ecosystems. To understand smoke's effects on climate and public
26 health, we analyzed the spatiotemporal distribution of smoke aerosols, focusing on two major
27 light-absorbing components, black carbon (BC) and brown carbon (BrC) aerosols. Using NASA's
28 Earth Polychromatic Imaging Camera (EPIC) instrument aboard the NOAA's Deep Space Climate
29 Observatory (DSCOVR) spacecraft, we inferred BC and BrC volume fractions and particle mass
30 concentrations based on spectral absorption provided by the Multi-Angle Implementation of
31 Atmospheric Correction (MAIAC) algorithm with 1-2 hours temporal resolution and ~10 km
32 spatial resolution over North America and Central Africa. Our analyses of regional smoke
33 properties reveal distinct characteristics for aerosol optical depth (AOD) at 443 nm, spectral single
34 scattering albedo (SSA), aerosol layer height (ALH), and BC and BrC amounts. Smoke cases in
35 North America show extremely high AOD up to 6, with elevated ALH (6-7 km) and significant
36 BrC components up to 250 mg/m² along the transport paths, whereas the smoke aerosols in Central
37 Africa exhibited stronger light absorption (i.e., lower SSA) and lower AOD, resulting in higher
38 BC mass concentrations and similar BrC mass concentrations than the cases in North America.
39 Seasonal burning source locations in Central Africa following the seasonal shift of Inter Tropical
40 Convergence Zone and diurnal variations in smoke amounts were also captured. Comparison of
41 retrieved AOD₄₄₃, SSA₄₄₃, SSA₆₈₀, and ALH with collocated AERONET and CALIOP
42 measurements shows agreement with *rmse* of 0.2, 0.03-0.04, 0.02-0.04, and 0.8-1.3 km,
43 respectively. Analysis of spatiotemporally average reveals distinct geographical characteristics in
44 smoke properties closely linked to burning types and meteorological conditions. Forest wildfires
45 over western North America generated smoke with small BC volume fraction of 0.011 and high
46 ALH with large variability (2.2 ± 1.2 km), whereas smoke from wildfires and agricultural burning
47 over Mexico region shows more absorption and low ALH. Smoke from savanna fires over Central
48 Africa has the most absorption with high BC volume fraction (0.015) and low ALH with small
49 variation (1.8 ± 0.6 km) among the analyzed regions. Tropical forest smoke was less absorbing
50 and had a high variance in ALH. We also quantify the estimation uncertainties related to the
51 assumptions of BC and BrC refractive indices. The MAIAC EPIC smoke properties with BC and
52 BrC volume and mass fractions and assessment of layer height provide observational constraints
53 for radiative forcing modeling and air quality and health studies.

54

55 **Keywords:** EPIC, light absorbing smoke aerosol component, BC, BrC

56



57 1. Introduction

58 Natural and anthropogenic fires affect and shape nearly every terrestrial vegetated
59 ecosystem on the planet (Pausas and Keeley, 2009; Bond and Keeley, 2005), and their emissions
60 have long been known to affect the global atmospheric composition and radiative budget (Hobbs
61 et al., 1997; Seiler and Crutzen, 1980). Recent climate changes and anthropogenic activities have
62 affected wildfire and agricultural fire occurrence in many regions (Liu et al., 2010; Dennison et
63 al., 2014). Global monitoring of atmospheric smoke aerosol chemical, optical, and microphysical
64 properties is important to quantify the impacts of increasing biomass burning on climate and air
65 quality. However, the current understanding of smoke aerosol radiative forcing is still insufficient
66 due to its high spatiotemporal variability in combination with the dynamic nature of smoke and
67 variability of its physical and optical properties (IPCC, 2023).

68 One characteristic that distinguishes smoke particle components from other components is
69 light absorption. Absorbing particle components converting incident electromagnetic energy into
70 thermal energy results in heating of both the particles and the ambient surrounding atmosphere.
71 Aerosol light absorption greatly affects direct radiative forcing and atmospheric stability and
72 convections (IPCC, 2023; Bellouin et al., 2005; Yu et al., 2002). Smoke particles emitted from
73 biomass burning typically contain two major light-absorbing carbonaceous components: black
74 carbon (BC) and brown carbon (BrC). The proportions of these light-absorbing components and
75 their mixing ratios determine the spectral absorption characteristics (e.g., Jacobson, 2001;
76 Chakrabarty et al., 2023).

77 BC is a byproduct of the incomplete combustion of carbonaceous materials. There is no
78 specific chemical makeup of BC and depending on measurement techniques it is also called soot,
79 elemental carbon, or light-absorbing carbon (Reid et al., 2005a; Moosmüller et al., 2009; Andreae
80 and Gelencsér, 2006). BC is visibly black, resulting in a high and spectrally invariant imaginary
81 refractive index (~ 0.79) across UV-visible wavelengths (Bond and Bergstrom, 2006). During
82 combustion, tiny BC spherules are aggregated with each other and grow by absorbing surrounding
83 gas-phase molecules into large particles with a complex, generally fractal-like morphology
84 (Moosmüller et al., 2009). Emitted atmospheric BC particles are generally hydrophobic (Petters et
85 al., 2009), but can quickly evolve to hydrophilic if they acquire water-soluble coatings upon
86 emission or during atmospheric aging (Tritscher et al., 2011). Atmospheric aging processes change
87 BC's physical and chemical particle structure (Corbin et al., 2023; Bhandari et al., 2019; Sengupta
88 et al., 2020), as well as optical properties (Gyawali et al., 2017; Kleinman et al., 2020; Reid et al.,
89 2005b). Particle evolutions combine with the high spatial and temporal variability of the sources
90 to make the net radiative effects of these particles highly uncertain (Bond et al., 2013; IPCC, 2023;
91 Chakrabarty et al., 2023).

92 The largest carbonaceous aerosol component directly emitted from biomass burning is
93 organic carbon (OC; e.g., Andreae and Merlet, 2001; Andreae, 2019 and references therein). This
94 study defines the OC with significant light absorbing property in the tropospheric solar spectrum
95 as brown carbon (BrC; e.g., Laskin et al., 2015). BrC exhibits spectral variability, absorbing more
96 ultraviolet (UV) and short visible light than long visible light, resulting in a reddish or brownish



97 appearance. Its imaginary refractive index varies spectrally, with generally higher values at shorter
98 (i.e., UV) wavelengths and decreasing toward longer, visible and infrared (IR) wavelengths
99 (Kirchstetter et al., 2004). BrC emission and the chemical processes responsible for BrC formation
100 are complex and not yet fully understood. Some studies suggest BrC consists primarily of water-
101 soluble organic carbon compounds and humic-like substances (Sun et al., 2007; Phillips and Smith,
102 2014; Hoffer et al., 2006) whereas others suggest that non-polar compounds can absorb more light
103 than polar compounds, especially in the UV and short-wavelength visible (Sengupta et al., 2018).
104 BrC compounds can be released from smoldering biomass burning or formed through secondary
105 organic aerosol processes in the atmosphere (Chakrabarty et al., 2010; Laskin et al., 2015). BC
106 coated with non-absorbing organic and inorganic may exhibit a similar wavelength dependence of
107 absorption, with higher values at shorter wavelengths (Wang et al., 2016). This similarity makes
108 it challenging to differentiate between BrC and coated BC based on spectral absorption alone.
109 Therefore, our "BrC" results may include contributions from coated BC.

110 According to the latest Intergovernmental Panel on Climate Change (IPCC) report (IPCC,
111 2023), the present day global effective radiative forcing of black carbon from fossil fuel and biofuel
112 is estimated at 0.107 W m^{-2} with a 5-95% uncertainty range of -0.202 to 0.417 W m^{-2} , with
113 respect to the pre-industrial time of 1750. In contrast, primary organic aerosols from fossil fuel
114 and biofuel, related to OC, exhibit a cooling effect of -0.209 W m^{-2} , with an uncertainty range of
115 -0.439 to -0.021 W m^{-2} . Although BrC is not directly considered in this assessment, its radiative
116 forcing is partially accounted for within primary organic aerosol, biomass burning, or secondary
117 organic aerosols in some global aerosol models. Combining ground-based measurements and
118 chemical transport modeling, Jo et al. (2016) attributed non-BC absorption to BrC and estimated
119 BrC fraction as 21% of the global mean surface OC concentration, significantly impacting ozone
120 photochemistry by altering the UV radiation field. Zhang et al. (2020) estimated that the global
121 BrC direct radiative effect is 0.10 W m^{-2} , suggesting that BrC can heat the tropical mid and upper
122 troposphere more than BC. Still, much uncertainty remains about BrC due to limited measurements
123 and the complex processes involved, challenging accurate estimates of its radiative impact on
124 climate (Liu et al., 2020).

125 Intensive *in situ* measurements have been instrumental in identifying the composition-
126 related spectral light-absorption properties of smoke plumes, as summarized in Bond and
127 Bergstrom (2006), Andreae and Gelencsér (2006), Moosmüller et al. (2009), and Samset et al.
128 (2018). These measurements have enabled remote sensing techniques to differentiate between
129 various light-absorbing components in smoke plumes. For example, the Aerosol Robotic Network
130 (AERONET) sunphotometers routinely provide aerosol optical and microphysical properties,
131 including spectral refractive indices from many sites worldwide (Holben et al., 1998; Dubovik and
132 King, 2000). Using AERONET inversion data, Schuster et al. (2016) inferred aerosol components
133 over smoke- and dust-dominated regions by matching AERONET spectral refractive index to
134 mixtures of components with different assumed optical properties. Specific absorbing components
135 were assumed as inclusions: BC and BrC for smoke and iron oxides of hematite and goethite for
136 dust aerosols. Wang et al. (2013) and Choi et al. (2020) applied a similar approach to East Asia



137 sites. The synergy between visible/near-IR AERONET measurement and UV/visible multifilter
138 rotating shadowband radiometer (MFRSR) measurements confirmed the sensitivity of spectral
139 absorption consistent with a BrC component (Mok et al., 2016, 2018).

140 Inferring aerosol composition from satellites is more challenging than from ground-based
141 remote sensing due to the need to account for the surface contribution to the top-of-atmosphere
142 signal, and the much greater range of conditions that space-borne instrument samples. Retrieving
143 aerosol absorptions using multi-spectral bands in near UV wavelengths has been applied to
144 instruments such as the Total Ozone Mapping Spectrometer (TOMS) and the Ozone Monitoring
145 Instrument (OMI), which have data records spanning decades, as well as more recently launched
146 instruments like the TROPOspheric Monitoring Instrument (TROPOMI) and Earth Polychromatic
147 Imaging Camera (EPIC; Torres et al., 1998, 2007, 2013, 2020; Ahn et al., 2021). The fraction of
148 retrieved single scattering albedo (SSA) within the expected error, defined as a fraction within
149 ± 0.03 from AERONET SSA, is approximately 50%, based on long-term and global validation
150 across these sensors (Ahn et al., 2021; Torres et al., 2020).

151 The Generalized Retrieval of Aerosol and Surface Properties (GRASP) algorithm
152 (Dubovik et al., 2011, 2014) utilizes the multi-angle, multi-channel, and both radiometric and
153 polarimetric measurements from the POLarization and Directionality of the Earth's Reflectances
154 (POLDER) instruments. With increased information incorporated by a multi-pixel multi-temporal
155 smoothness constraint, the GRASP algorithm retrieves aerosol optical depth (AOD), particle size
156 information, and absorption, showing robust agreement with global AERONET measurements
157 (Chen et al., 2020). Recent improvement of the GRASP algorithm included the direct estimation
158 of aerosol chemical composition concentrations without the need for intermediate steps such as
159 retrieving refractive indices and particle size distributions (Li et al., 2019, 2020). The Multi-angle
160 Imaging SpectroRadiometer (MISR) research algorithm also accounts for black-smoke and brown-
161 smoke aerosol models (Limbacher et al., 2022), analogous to the BC and BrC components in this
162 study, and is utilized to analyze fractional AODs along transport paths (Jungheun Noyes et al.,
163 2020a, b, 2022). Still, it is worth noting that POLDER and MISR measurements are limited to
164 visible and near-infrared (NIR) channels and do not include ultraviolet (UV) channels, where
165 spectral absorption due to BC and in particular BrC is more pronounced.

166 The EPIC sensor aboard the Deep Space Climate Observatory (DSCOVR) spacecraft has
167 provided UV-near IR measurements of Earth since 2015 (Marshak et al., 2018). Recent studies by
168 (Lyapustin et al., 2021b) have utilized the Multi-Angle Implementation of Atmospheric Correction
169 (MAIAC) processing of EPIC measurements to derive AOD and spectral absorption. It enables
170 inferring aerosol chemical compositional differences, such as BC and BrC in smoke aerosol
171 plumes and iron oxides (e.g., hematite and goethite) in dust aerosol plumes. DSCOVR's orbit
172 around the Lagrange-1 point, where the spacecraft remains stably positioned between the sun and
173 Earth, allows for global monitoring multiple times per day during the daylight time with a temporal
174 resolution of 1-2 hours. In our study, we used EPIC measurements to infer BC and BrC volume
175 fractions and mass concentrations in smoke plumes and identified distinct smoke properties over



176 North America and Central Africa. The estimation of iron oxides in dust aerosols using the EPIC
177 MAIAC product was addressed in Go et al. (2022).

178 The structure of the paper is as follows. Section 2 introduces the EPIC MAIAC smoke
179 aerosol retrieval algorithm and describes the methodology for inferring BC and BrC volume
180 fractions and mass concentrations. It also includes descriptions of study regions and of AERONET
181 and CALIOP validation datasets. In Section 3, we analyzed individual smoke cases over North
182 America and Central Africa, and provided validation of AOD, spectral SSA, and aerosol layer
183 height (ALH). Additionally, time-integrated regional properties, including BrC/BC ratios, and
184 uncertainty estimates based on different inclusion assumptions are discussed. Finally, Section 4
185 offers summary and concluding remarks.

186 2. Data and methods

187 2.1 MAIAC EPIC processing algorithm

188 EPIC measurements cover the entire sunlit hemisphere of Earth with ten narrowband
189 spectral channels from 317.5 to 779.5 nm. The spatial resolution of EPIC is ~8-16 km at nadir,
190 degrading toward the edge of the image. MAIAC EPIC algorithm grids and processes L1B data at
191 10 km resolution providing an oversampling. DSCOVR's Lagrange point 1 orbit between the Earth
192 and the Sun (~1.5 million kilometers) enables global multi-temporal daytime measurements, with
193 10–12 observations in boreal summer and 6-7 observations in winter at mid-latitudes and little
194 seasonal change in tropical latitudes. Detailed information on EPIC measurements can be found
195 in Marshak et al. (2018). Following the MAIAC Moderate Resolution Imaging Spectroradiometer
196 (MODIS) algorithm (Lyapustin et al., 2018), the standard MAIAC processing offers cloud
197 detection, atmospheric correction, and AOD with regionally specified background aerosol models
198 (“background AOD”; Lyapustin et al., 2021a). In addition, a newly developed absorbing smoke or
199 dust aerosol retrieval process was applied to both land and ocean pixels. Smoke/dust detection and
200 separation are based on various tests including UV aerosol index and spectral AOD shape. As
201 EPIC band configuration does not allow to distinguish between smoke and dust aerosols, the dust
202 retrievals are only performed over pre-defined dust regions whereas smoke retrievals are
203 performed elsewhere globally (Lyapustin et al., 2021b).

204 The full algorithm description is given elsewhere (Lyapustin et al., in preparation); here
205 we provide a very brief overview to facilitate understanding of our results. The novel version 3
206 (v3) MAIAC algorithm represents spectral aerosol absorption with two parameters, the imaginary
207 refractive index at 680 nm (k_0) and spectral absorption exponent (SAE), using a conventional
208 power-law expression, $k_\lambda = k_0(\lambda/\lambda_0)^{-SAE}$ where $\lambda_0 = 680$ nm. The real refractive index is
209 assumed to have a spectrally invariant value of 1.51 (Lyapustin et al., 2021b). The particle log-

210 normal volume size distribution is defined as $\frac{dV(r)}{d\ln(r)} = \sum_{i=1}^2 \frac{C_{Vi}}{\sqrt{2\pi}\sigma_i} e^{-\frac{1}{2}\left(\frac{\ln(r)-\ln(r_{v,i})}{\sigma_i}\right)^2}$, where i

211 indicates each mode (fine and coarse), r is the particle radius, $r_{v,i}$ is the volume mean radius, σ_i is



212 the geometric standard deviation, $c_{v,i}$ is the volumetric concentration. For smoke aerosols, we
213 assumed fine mode volume mean radius (0.14 μm) and geometric standard deviation (0.4 μm),
214 coarse mode volumetric mean radius (2.8 μm) and geometric standard deviation (0.6 μm). In
215 MAIAC v3, the Levenberg-Marquardt nonlinear optimal fitting algorithm (Levenberg, 1944;
216 Marquardt, 1963) is used to simultaneously retrieve four parameters {AOD₄₄₃, k_0 , SAE, ALH} by
217 matching EPIC measurements at UV to NIR wavelengths, including oxygen A and B bands. The
218 algorithm uses pre-computed look-up tables (LUTs) covering the full range of expected variability
219 of the above parameters. The maximum value of AOD at 443 nm in the algorithm is set to 6.
220 Vertically, the aerosol is modeled by a single 2 km-thick aerosol layer placed at different altitudes
221 in the atmosphere, and the reported ALH is defined as the midpoint height of the layer. To avoid
222 systemic biases in absorption, this retrieval is performed over detected absorbing smoke/dust
223 pixels when the retrieved AOD, based on the background aerosol model with fixed regional
224 properties, is greater than 0.4. Note that although smoke retrievals are limited with “background
225 AOD₄₄₃ > 0.4” the retrieved smoke AOD₄₄₃ could be lower than 0.4 due to different assumption
226 of microphysical properties and simultaneous retrieval of spectral absorption and ALH.

227 **2.2 MAIAC smoke composition inference**

228 Given a very different spectral absorption of BC (high and spectrally fairly flat) and BrC
229 (low and strongly increasing towards UV), the retrieved spectral absorption can be used to derive
230 fractions of absorbing components. We assume that smoke aerosols consist of a non-absorbing
231 host and two absorbing species, BC and BrC, with internal mixing based on Maxwell Garnett
232 effective medium approximation (MG-EMA) (Bohren and Huffman, 1998; Schuster et al., 2005,
233 2016). The MG-EMA is suitable for characterizing smoke particles and is computationally
234 efficient (Garnett, 1904; Bohren and Huffman, 1998; Schuster et al., 2005; Markel, 2016a, b). For
235 that reason, it is widely used for inferring aerosol compositions from ground-based or satellite-
236 based remote sensing (Li et al., 2019; Schuster et al., 2005, 2016; Choi et al., 2020; Go et al., 2022).
237 Studies showed that different mixing rules, such as Bruggeman approximation or volume
238 averaging, yields similar results to the MG-EMA for inferring smoke components (Schuster et al.,
239 2016; Li et al., 2019; and references therein). The non-absorbing host (or medium) represents a
240 mixture of non-absorbing or low-absorbing components in smoke, such as non-absorbing OC,
241 sulfate, nitrate, and/or ammonium. Although there are various ranges of refractive indices for both
242 BC and BrC based on literature and experiments, this study assumes fixed refractive index to
243 estimate their fractions from the limited information of the retrieved optical properties. The BC
244 refractive index assumes Bond and Bergstrom (2006)’s suggestion of spectrally flat with a real
245 part (n) of 1.95 and an imaginary part (k) of 0.79 for the visible spectrum (i.e., 400 – 700 nm).
246 Spectral dependence of k for BrC is based on Kirchstetter et al. (2004), whereas a constant real
247 part of 1.54 was assumed based on Li et al. (2019). For a spectrally flat and non-absorbing host
248 we assume $n=1.51$, consistent with the smoke aerosol model in the MAIAC EPIC algorithm, and
249 $k=10^{-9}$ based on Kalashnikova et al. (2018). Table 1 summarizes the spectral refractive indices of



250 BC, BrC and host. Please note that a sensitivity test for different assumptions regarding BC and
 251 BrC imaginary refractive indices affecting their volume fractions is detailed in Sec 3.5.

252

253 Table 1. Spectral refractive indices of smoke aerosol components at EPIC wavelengths.

Wavelengths (nm)	BC		BrC		host	
	n	k	n	k	n	k
340	1.95	0.790	1.54	0.187	1.51	10 ⁻⁹
388	1.95	0.790	1.54	0.125	1.51	10 ⁻⁹
443	1.95	0.790	1.54	0.070	1.51	10 ⁻⁹
680	1.95	0.790	1.54	0.003	1.51	10 ⁻⁹

254

255 The MG-EMA equation for smoke aerosol mixtures, as described in Bohren and Huffman
 256 (1998) and Schuster et al., (2005), is presented below.

257
$$\epsilon_m = \epsilon_h \left[1 + \frac{3 \left(f_{BC} \frac{\epsilon_{BC} - \epsilon_h}{\epsilon_{BC} + 2\epsilon_h} + f_{BrC} \frac{\epsilon_{BrC} - \epsilon_h}{\epsilon_{BrC} + 2\epsilon_h} \right)}{1 - f_{BC} \frac{\epsilon_{BC} - \epsilon_h}{\epsilon_{BC} + 2\epsilon_h} - f_{BrC} \frac{\epsilon_{BrC} - \epsilon_h}{\epsilon_{BrC} + 2\epsilon_h}} \right]$$

258

259 Here, ϵ_m , ϵ_h , ϵ_{BC} , and ϵ_{BrC} represent the complex dielectric functions of the mixture, host,
 260 BC, and BrC, respectively, and f_{BC} and f_{BrC} denote the volume fractions of BC and BrC,
 261 respectively. Note that identical BC and BrC components are assumed for both fine and coarse
 262 modes. Throughout plume evolution, different processes such as oxidation, hydration, deposition
 263 of volatile organics onto existing particles, or new particle formation, may lead to larger particle
 264 sizes. Consequently, the fine-mode and coarse-mode components in smoke aerosols could exhibit
 265 differences. Schuster et al. (2016) also accounted for different component combinations between
 266 fine and coarse modes, considering dust particles for the coarse mode. It should be noted that
 267 biomass burning aerosols are strongly dominated by the fine mode component, with typically only
 268 a minor coarse mode AOD. However, the MAIAC EPIC processing relies on a static particle size
 269 distribution, and dynamic separation of fine and coarse modes is challenging with limited
 measurement information.

270

The refractive indices of the mixture can be determined using the following equations:

271

$$n = \sqrt{\frac{\epsilon_r^2 + \epsilon_i^2 + \epsilon_r}{2}},$$

272

$$k = \sqrt{\frac{\epsilon_r^2 + \epsilon_i^2 - \epsilon_r}{2}},$$



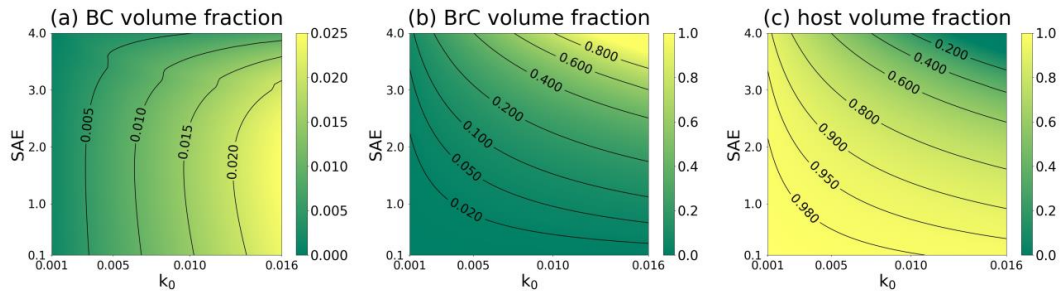
273 where ϵ_r and ϵ_i represent the real and imaginary parts of the mixture dielectric function ϵ_m . Given
 274 fixed spectral refractive indices of the host and inclusions (BC and BrC), the mixture refractive
 275 indices are determined by the volume fractions of two inclusions (f_{BC} and f_{BrC}).

276 Subsequently, we utilized the Levenberg-Marquardt nonlinear least-square fitting method
 277 (Levenberg, 1944; Marquardt, 1963; Press et al., 2007) to derive the volume fractions of inclusions
 278 by comparing inferred and calculated refractive indices with the MG-EMA. Retrieved k_0 and SAE
 279 were converted into spectral imaginary refractive indices (k_λ for λ of 340, 380, 443, and 680 nm)
 280 and matched with theoretical values of a mixture to find solutions for f_{BC} and f_{BrC} .

281 Fig. 1 illustrates the derivable BC, BrC, and host volume fractions for assumed ranges of
 282 k_0 (0.001–0.016) and SAE (0.1–4) in the MAIAC EPIC algorithm. Available f_{BC} , f_{BrC} , and f_{host}
 283 ranges are from 0 to 0.025, 0.994, and 0.998, respectively, where $f_{host} = 1 - f_{BC} - f_{BrC}$. The
 284 maximum f_{BC} of 0.025 can be found in the condition of maximum k_0 of 0.016. A high f_{BrC} near
 285 one can be retrieved when both k_0 and SAE are high. The host volume fraction (f_{host}) shows an
 286 opposite tendency to f_{BrC} and is low when both k_0 and SAE are high. Conversion from retrieved
 287 k_0 and SAE to volume fractions follows the presented distributions.

288 It should be mentioned that the upper limit of $k_0=0.016$ was found empirically based on
 289 limited EPIC regional processing, and then confirmed by the global processing of EPIC data.
 290 However, this limit may be increased in the future based on detailed analysis of EPIC retrievals,
 291 in particular because AERONET inversion retrievals often show higher values, for example in
 292 Central and southern Africa savanna burning region (Eck et al., 2003).

293



294

295 Figure 1. The range of volume fractions for (a) BC, (b) BrC, and (c) host across different values
 296 of k_0 and SAE.

297

298 The inferred volume fractions of BC and BrC can be converted to column-integrated
 299 volume concentrations as,

300

$$C_V = C_{Vf} + C_{Vc} = \frac{AOD_f}{h_f} + \frac{AOD_c}{h_c},$$

301

$$AOD_f = AOD \cdot \left(\frac{C_{Vf}}{C_{Vf} + C_{Vc}} \right),$$

302

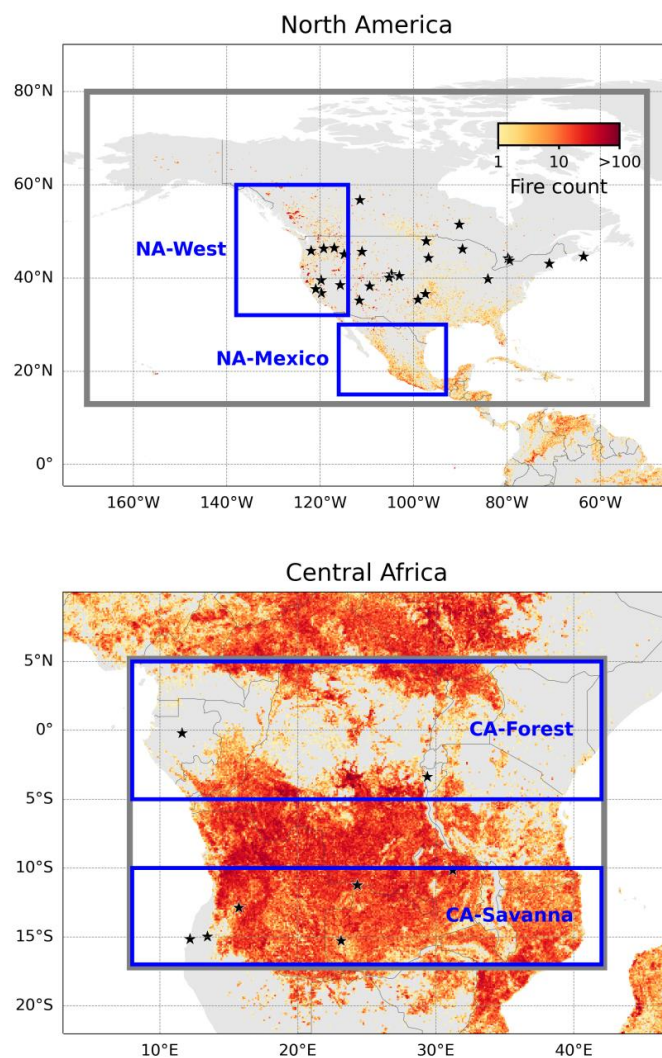
$$AOD_c = AOD \cdot \left(\frac{C_{Vc}}{C_{Vf} + C_{Vc}} \right),$$



303 where C_V is the column-integrated volume concentration with a unit of $\mu\text{m}^3/\mu\text{m}^2$, the subscripts f
304 and c indicate fine-mode and coarse-mode, respectively. Despite the regional dependence of $\frac{C_{Vc}}{C_{Vf}}$
305 in the 4D-retrieval algorithm for smoke, we assume a static $\frac{C_{Vc}}{C_{Vf}}$ of 0.7 for BC and BrC processing
306 to maintain consistency and reduce regional discrepancies arising from the ratio. Hygroscopicity
307 was neglected by using a static AOD per volume concentration regardless of relative humidity.
308 Given the size distribution and n , h_f of $8.43 \mu\text{m}^2/\mu\text{m}^3$ is fine mode AOD_{443} per unit volume
309 concentration ($\mu\text{m}^3/\mu\text{m}^2$) and h_c of $0.72 \mu\text{m}^2/\mu\text{m}^3$ is coarse mode AOD_{443} per unit volume
310 concentration, as calculated based on Mie theory in the MAIC EPIC smoke model (Lyapustin et
311 al., 2021b). Given the complex refractive indices, size distribution with fine-mode or coarse-mode
312 only, and non-sphericity, the h values, representing total column AOD per unit volume
313 concentration, are computed using the DLS (sphere and spheroid) model (Dubovik et al., 2006) at
314 volume concentration of $1 \mu\text{m}^3/\mu\text{m}^2$. h_f and h_c are computed separately for the fine and coarse
315 modes within the MAIAC look-up table generation package and can be used to assess mass
316 extinction efficiency (MEE) with assumption of particle density. The column-integrated mass
317 concentration of the chemical component is calculated as $C_{M,i} = C_V \cdot f_i \cdot \rho_i$, where i indicates
318 inclusions (BC and BrC) and ρ is mass concentration per unit volume. We use ρ_{BC} of 1.8 g/cm^3
319 and ρ_{BrC} of 1.2 g/cm^3 following previous studies (Bond and Bergstrom, 2006; Turpin and Lim,
320 2001; Schuster et al., 2016; Li et al., 2020).

321 2.3 Study regions

322 We selected two major regions where smoke aerosols are dominant but exhibit different
323 characteristics: North America (170°W - 50°W and 13°N - 80°N) and Central Africa (8°E - 42°E and
324 17°S - 5°N). To avoid potential interference from dust aerosols on smoke analysis, we excluded the
325 Sahel region bounding the Sahara Desert from this study. The selected smoke aerosol analysis
326 regions, along with detected fire counts from the Visible Infrared Imaging Radiometer Suite
327 (VIIRS) instrument onboard the Suomi National Polar-orbiting Partnership (SNPP) satellite in
328 2018, are presented in Fig 2. This study focused on the entire year of 2018, a year marked by one
329 of highest monthly average AOD during the summer over North America (Eck et al., 2023). The
330 EPIC dataset exhibited no temporal gaps, and ample AERONET and CALIOP data were
331 accessible. Additionally, we included a single case study from 2017 to complement our analysis
332 over North America.



333
334 Figure 2. Cumulative fire detection counts from VIIRS within a 0.1° by 0.1° longitude-latitude
335 grid in 2018 over North America and Central Africa. The study regions are denoted by grey
336 rectangles, and AERONET locations are marked with blue stars. Subregions including western
337 (“NA-West”) and Mexico (“NA-Mexico”) in North America, as well as tropical forest (“CA-
338 Forest”) and savanna (“CA-Savanna”) regions in Central Africa are denoted by blue rectangles.

339 2.4 AERONET

340 In order to evaluate the EPIC-retrieved AOD and spectral absorption, we utilized the
341 Version 3 Level 2.0 AERONET Inversion dataset (Holben et al., 1998; Dubovik and King, 2000;



342 Giles et al., 2019; Sinyuk et al., 2020). The EPIC-retrieved AOD₄₄₃, SSA₄₄₃ and SSA₆₈₀ were
343 compared with the AERONET counterpart derived from direct and sky radiance measurements.
344 The AERONET measurements of spectral AOD have accuracy of ~0.01 to 0.02 at optical air mass
345 of one with higher uncertainty in the UV (Eck et al., 1999). The AERONET retrieved SSA at 440
346 nm have uncertainty of ~0.03 at AOD(440)=0.4 with smaller uncertainties at larger AOD,
347 decreasing to ~0.015 at AOD(440)=1.3 for biomass burning aerosols at the Mongu, Zambia site
348 (Sinyuk et al., 2020). Spatiotemporal collocation between AERONET and EPIC measurements
349 was conducted as follows: (1) averaging AERONET AOD within a ±30-min range and averaging
350 SSA within a ±3-hour range from the EPIC measurement time, and (2) averaging EPIC 5 × 5 pixels
351 (~50 × 50 km²) collocated with the AERONET sites and limited to cosines of solar zenith angle
352 and view zenith angle above 0.45 (i.e., solar zenith angle & view zenith angle < 63.3°). The EPIC
353 pixels were spatially averaged when at least 50% of EPIC smoke products are valid in the spatial
354 window. AERONET retrievals with extinction Ångström exponent between 440 and 675 nm
355 greater than 0.4 were selected to avoid possible dust contamination. SSA validation was conducted
356 only when AERONET AOD at 440 nm was greater than 0.6. The AERONET sites with at least
357 five measurements available were considered. Consequently, a total of 28 and 7 AERONET sites
358 were chosen over North America and Central Africa, respectively (see Fig 2).

359 **2.5 CALIOP**

360 The Cloud-Aerosol Lidar with Orthogonal Polarization (CALIOP) onboard Cloud-Aerosol
361 Lidar and Infrared Pathfinder Satellite Observations (CALIPSO) satellite has provided global
362 measurements of aerosol vertical distribution. We collected profiles of total attenuated backscatter
363 coefficients at 532 nm (β , unit of km⁻¹sr⁻¹) from the CALIPSO Lidar Level 2 Aerosol Profile
364 version 4.51 dataset (“CAL_LID_L2_05kmAPro-Standard-V4-51”) in 2018. Subsequently, we
365 calculated backscatter-weighted aerosol layer height using the formula $ALH_{CALIOP} = \frac{\sum \beta z}{\sum \beta}$, where
366 z represents the height of each layer. This definition is widely employed for validating aerosol
367 layer height using CALIOP (Go et al., 2020; Xu et al., 2019). The ALH_{CALIOP} data within a ±30
368 min from EPIC acquisitions were spatially averaged within MAIAC EPIC grid. We used the same
369 cutoff threshold for the Sun and view zenith angle as above. To mitigate ALH uncertainty for weak
370 aerosol cases, the ALH comparison was conducted when CALIOP AOD at 532 nm exceeded 0.6.

371 **3. Results**

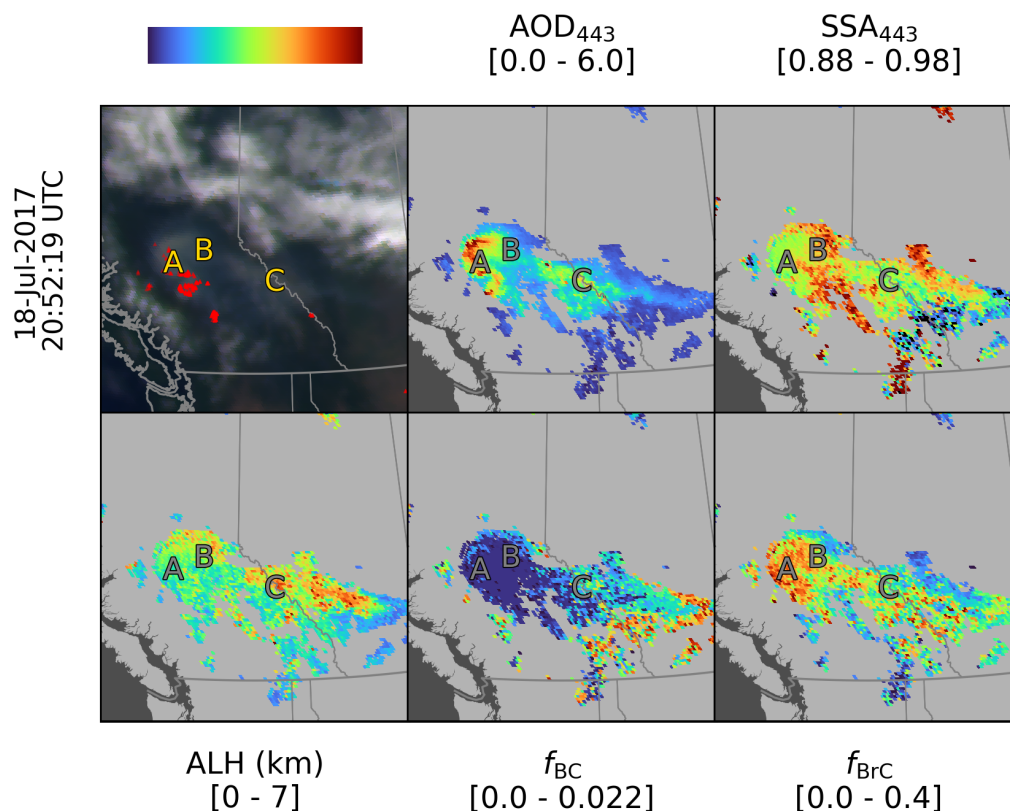
372 **3.1 Analysis of individual cases**

373 **3.1.1 North America**

374 Western North America stands out as one of the most active wildfire regions globally. For
375 our analysis, we selected an intense wildfire and associated smoke aerosol event occurring on July
376 18, 2017, at 20:52:19 Coordinated Universal Time (UTC) over western Canada in Fig 3. Note that

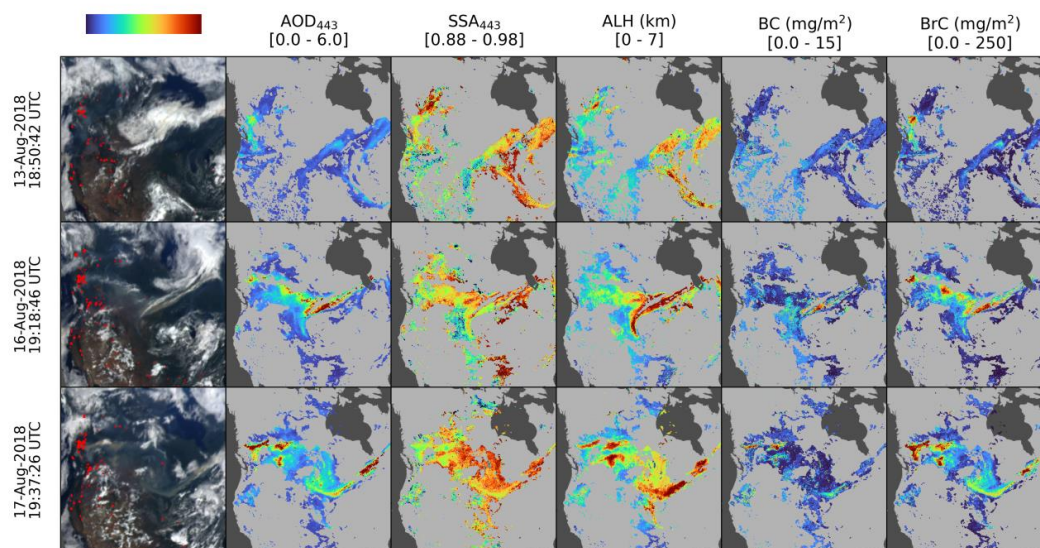


377 all other analyses in this study are for 2018 except for this case. Utilizing the VIIRS/SNPP Thermal
378 Anomalies/Fire (Schroeder and Giglio, 2018), visualized as red dots within the true-color images,
379 we identified wildfires in British Columbia. The true-color image and retrieved smoke particle
380 properties illustrate the eastward transport of the smoke plume. Specifically, pixels near the
381 wildfires (region “A” in Fig 3) exhibited AOD₄₄₃ nearing ~4-6, alongside an SSA₄₄₃ of ~0.93.
382 Pixels approximately 50~100 km from the sources (region “B”), show decreased AOD₄₄₃ (~2) and
383 less absorption (SSA₄₄₃ of ~0.96). Notably, the contrast in SSA is more pronounced at 388 nm
384 than at 680 nm (not shown). Absorption changes within this distance are related to the aging
385 process. Freshly emitted particles from wildfires exist in various mixing states and undergo
386 multiple processes, such as coagulation, condensation/evaporation, oxidation, and secondary
387 aerosol particles formed from chemical production (Reid et al., 2005a, b; Liu et al., 2020). Smoke
388 aerosol mixtures become less absorbing in the UV and shortwave visible wavelengths when
389 transported from sources through these aging processes, consistent with findings from other *in-*
390 *situ* and remote sensing measurement studies (Junghenn Noyes et al., 2020a, b; Kleinman et al.,
391 2020). The increased SSA₄₄₃ from 0.93 to 0.96 (from region “A” to “B”) corresponds to a decrease
392 in the BrC fraction from 0.3 to 0.1. Aerosol plumes over Alberta, farther downwind to the east
393 (region “C”), exhibited a) high AOD₄₄₃ values (1-3), b) SSA₄₄₃ of ~0.92-0.94, c) increased BC
394 volume fraction up to 0.01; and d) a similar BrC volume fraction (about 0.3 at the plume center)
395 for pixels close to the fire sources. The eastern part of the plumes was located farther away from
396 the source and could have undergone more extensive aging. Smoke aerosol near sources was
397 located close to the surface (ALH above sea level of ~1 km) and was elevated to about 5-6 km in
398 the downwind area. It is important to consider that the fires could also undergo various stages of
399 combustion intensity over time, which could also be a factor in BC and BrC production. The
400 observed differences in ALH suggest that possibly some of these fires were more intense earlier,
401 leading to the lofting of the plume to 5-6 km. Subsequently, the intensity may have decreased,
402 resulting in a lower ALH as the plume transitioned to a more smoldering phase. This scenario,
403 particularly applicable to long plume lengths, implies that fire intensity and the relative combustion
404 fraction (flaming/smoldering) likely varied over the course of several hours during the transport
405 of such a long plume distance.



406
 407 Figure 3. Illustration of EPIC smoke aerosol optical properties over western North America on
 408 July 18, 2017. Red dots in the first left panel are VIIRS/NPP thermal anomaly hotspots. The
 409 underlying image and analyses in subsequent panels correspond to EPIC true color and MAIAC
 410 EPIC retrievals (AOD_{443} , SSA_{443} , and ALH) with inferred BC and BrC volume fractions. The color
 411 bar scale is indicated at the top of each panel.

412
 413 Continental-scale smoke aerosol episodes in August 2018, derived from the analysis of
 414 Lyapustin et al. (2021b), are depicted in Fig 4. On August 13 (top panels), smoke aerosol plumes
 415 along the west coast of North America, near the detected wildfire sources, exhibit high AOD of
 416 nearly 3-4 and SSA_{443} of 0.93 in the plume center. Surrounding pixels of the plume generally show
 417 lower AOD and higher SSA than the pixels interior to the plume. Subsequently, westerly
 418 transported plumes with increased AOD (up to ~6) and ALH (~6-7 km) were detected on August
 419 16 and 17. Corresponding BC and BrC fractions ranged from 0.005 to 0.01 and 0.2 to 0.3 (not
 420 shown), with column mass concentrations reaching 15 mg/m^2 and 250 mg/m^2 , respectively.

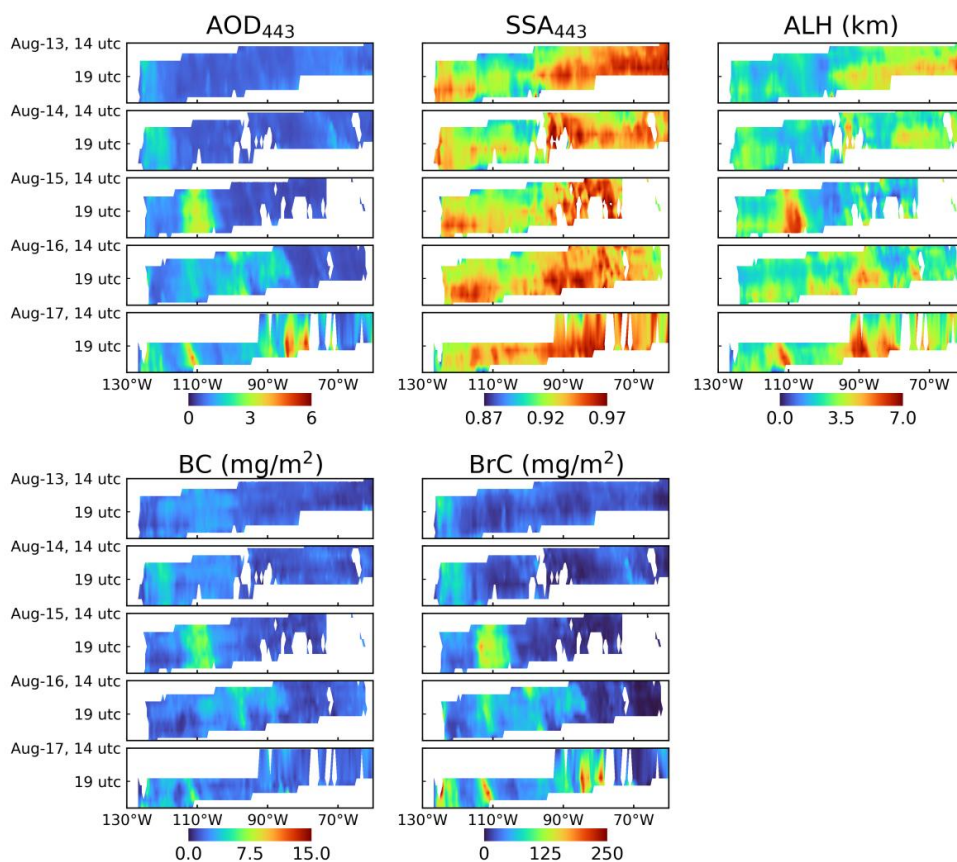


421

422 Figure 4. Illustration of smoke aerosol optical properties (AOD₄₄₃, SSA₄₄₃, ALH, and BC and BrC
423 mass concentrations) over North America on August 13, 16, and 17, 2018. The color bar scale is
424 indicated at the top of each panel.

425

426 EPIC can effectively monitor the change of smoke optical properties during transport at
427 high temporal cadence. Meridional averages of AOD₄₄₃, SSA₄₄₃, ALH, and BC and BrC mass
428 concentrations over the period from August 13 to 17, 2018 are represented as Hovmöller diagrams
429 in Fig 5. Plume evolution is clearly captured, with a temporal resolution of 1-2 hours, from initial
430 smoke aerosol emission over western North America, to subsequent transport toward the east with
431 an increased ALH from ~1 km to 6-7 km, and eventually to dispersion.



432

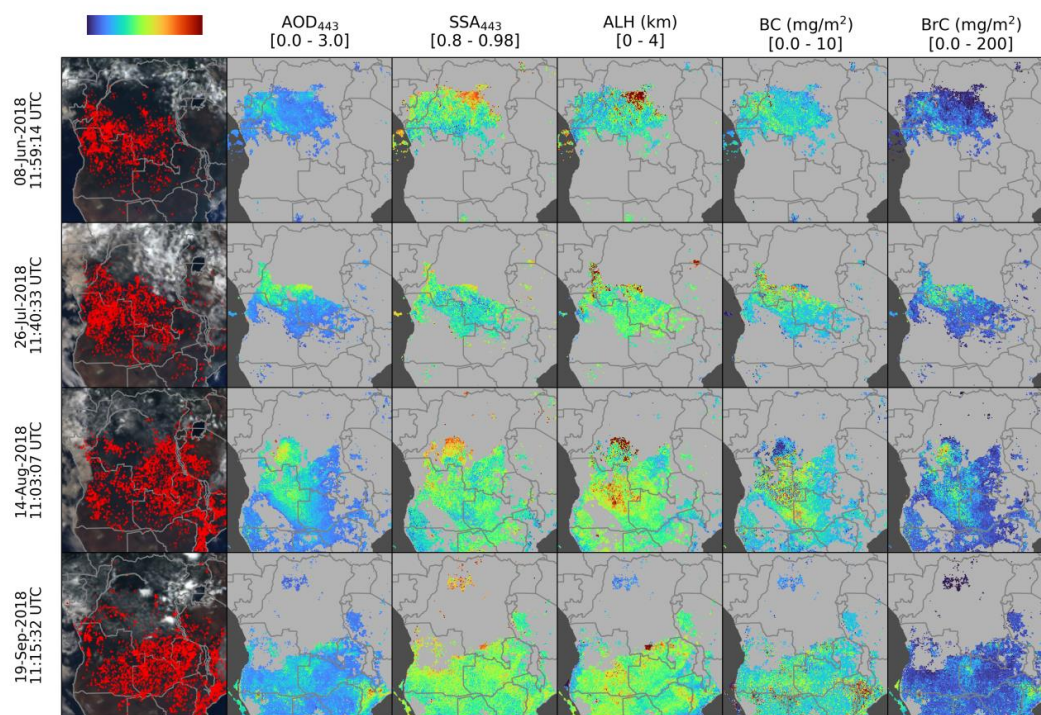
433 Figure 5. Hovmöller diagrams of AOD₄₄₃, SSA₄₄₃, ALH, and BC and BrC volume fractions over
 434 North America (130-60°W, 25-53°N, 0.5° longitudinal interval) from August 13 to 17, 2018. Gaps
 435 in the data are due to low AOD or meteorological clouds.

436 3.1.2 Central Africa

437 Biomass burning over Central Africa generates smoke aerosols with distinct optical
 438 properties. Long-term AERONET measurements over Southern Africa savanna regions indicate
 439 the strongest absorption among global smoke regions, with SSA values at 440 and 680 nm of 0.87
 440 and 0.86, respectively (Dubovik et al., 2002; Giles et al., 2012; Sayer et al., 2014). The biomass
 441 burning emission pattern in Africa follows a clearly defined seasonal cycle, influenced by
 442 precipitation linked to the seasonal movement of the Inter-Tropical Convergence Zone (ITCZ)
 443 (Swap et al., 2003). There exists a strong temporal cycle of SSA as well, with the lowest SSA
 444 values in June due to savanna burning, and increasing through October as more forested areas burn



445 (Eck et al., 2013). And yet, particle size distributions tend to remain unchanged (Reid et al., 2005b;
 446 Sayer et al., 2014). This makes the region an ideal test environment for absorption retrievals. We
 447 selected four cases (June 8, July 26, August 14, and September 19, 2018) to illustrate the seasonal
 448 changes in smoke regions from northeast to southwest; these align closely with the climatological
 449 patterns detected by other ground-based and satellite measurements (Eck et al., 2013; Duncan et
 450 al., 2003). The detected fires were subcontinent-wide (Fig 6) and generated smoke with AOD
 451 reaching up to ~ 2 . The general particle properties were consistent across the four cases. The light
 452 absorption, reaching as low as ~ 0.84 SSA_{443} , was notably stronger than in the cases over North
 453 America. The ALH of pixels with high AOD remained relatively constant at 2-3 km. High BC
 454 concentrations (e.g., > 5 mg/m^2) were prevalent over detected fire locations despite relatively
 455 lower AOD condition (e.g., $AOD_{443} < 2$) than in the cases over North America, where similar BC
 456 concentrations were observed from the pixels with $AOD_{443} > \sim 3$.
 457

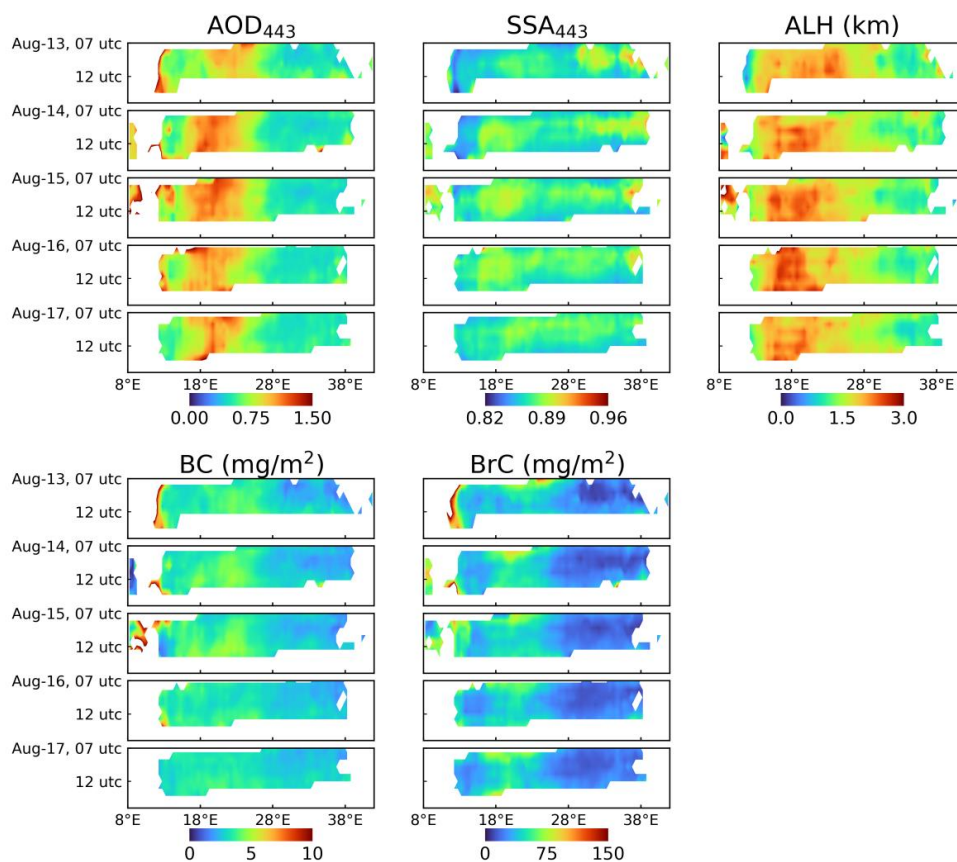


458
 459 Figure 6. Illustration of smoke optical properties (AOD_{443} , SSA_{443} , ALH, and BC and BrC mass
 460 concentrations) over Central Africa on June 8, July 26, August 14, and September 19, 2018.
 461

462 The measurements taken over five consecutive days from August 13-17 over the Central
 463 Africa study region detected weaker zonal smoke plume transport with less dynamic changes in
 464 particle properties (Fig 7) compared to the North America cases (Fig 5). The relatively low ALH



465 of 2-3 km indicates that smoke aerosol mostly concentrated within the boundary layer and was
 466 less influenced by strong jets at higher altitudes. AOD was slightly enhanced during early morning
 467 and late afternoon by ~10-20% over 20-25°E region. The afternoon pattern is consistent with long-
 468 term AERONET measurements shown in Eck et al. (2003), whereas the morning pattern should
 469 be further analyzed. From SEVIRI measurements, the peak of active fires is most frequently
 470 detected around noon (Wooster et al., 2021). Eck et al. (2003) concluded that elevated air
 471 temperatures, reduced relative humidity, and heightened wind speeds during the midday and
 472 afternoon periods often lead to more intense and rapidly spreading fires.



473
 474 Figure 7. Same with Fig 5 except for over Central Africa (8-42°E, 17°S-5°N, 0.5° longitudinal
 475 interval) from 13 to 17 August 2018.

476
 477 The observed difference between the two regions clearly correlates with the different fuel
 478 types – forests in North America and savannah grasses and bushes in Central Africa. For instance,



479 forest wildfires in North America with much higher thermal energy density result in elevated ALH,
480 incomplete combustion, and higher BrC concentrations, whereas fast-spreading grassland fires are
481 known for high BC concentration from flaming combustion emissions, but lower energy density,
482 which keep generated smoke generally within the boundary layer over Central Africa.

483 **3.2 Comparison of smoke properties derived from AERONET and CALIOP**

484 The regional validation of AOD, spectral SSA, and ALH throughout 2018 using the
485 AERONET and CALIOP datasets is presented in Fig 8. The AOD comparison over North America
486 demonstrates a correlation coefficient (R) of 0.91 and a root mean squared error ($rmse$) of 0.22. It
487 is important to note that this comparison only covers smoke retrievals; it excludes low AOD
488 conditions (e.g., background AOD at 443 nm < 0.4), that may result in lower validation statistics
489 compared to the previous analysis incorporating the combined “background+smoke” AOD (R of
490 0.85 and $rmse$ of 0.13 in Lyapustin et al., 2021b). Nonetheless, the mean bias error (MBE) of 0.02
491 in version 3 is smaller than the 0.05 reported by Lyapustin et al. (2021b) based on v2. The fraction
492 within expected error ($EE\%$), defined as $\pm(0.05+0.2\times\text{AERONET AOD})$, is 74.9%. Central Africa
493 AOD also exhibits similar validation statistics, except for a lower R (0.60), likely due to a narrow
494 range of collocated AOD compared to North America. However, the MBE of -0.04 and $EE\%$ of
495 74.8% are comparable to the statistics for North America. Despite the absence of IR channels for
496 cloud detection and the relatively coarse spatial resolution (>10 km) of EPIC, which can lead to
497 sub-pixel cloud contamination (Marshak et al., 2018), the achieved accuracy in AOD retrieval is
498 very encouraging.

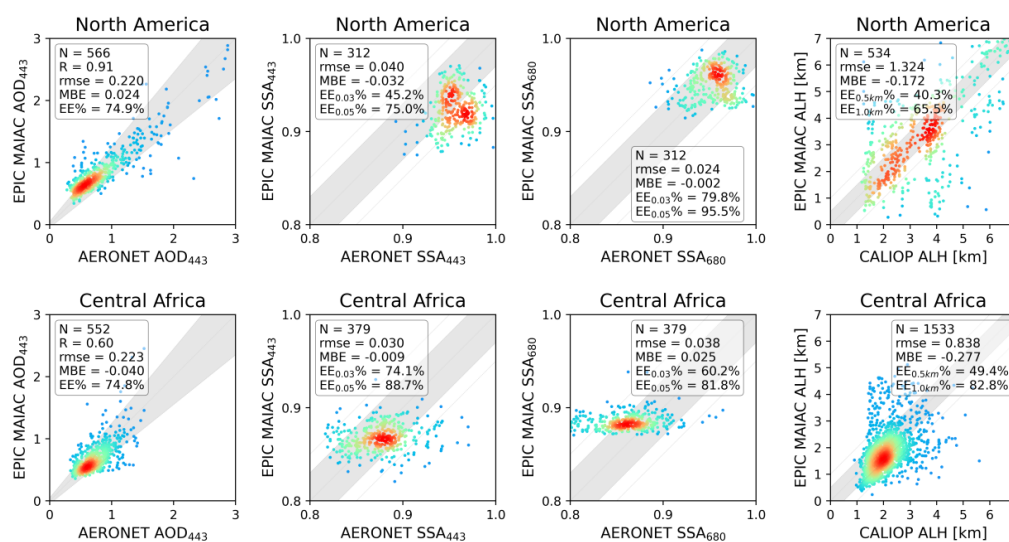
499 Regional comparisons of SSA with AERONET retrievals are more distinct than those of
500 AOD. Overall, the SSA_{443} over North America from EPIC is lower than that from AERONET with
501 MBE of -0.03 and EE fraction (within $\pm 0.03 + \text{AERONET SSA}$; $EE_{0.03}\%$) of 45.2%. The
502 collocated range spans about 0.88 to 0.97 from EPIC and 0.90-1.00 from AERONET.
503 Comparisons over Central Africa show a much smaller bias (MBE of -0.01) and higher $EE_{0.03}\%$
504 of 74.1%. The regional difference in accuracy could be attributed to uncertainty in our assumptions
505 of regional smoke model properties (e.g., particle size and real refractive index). Nonetheless, the
506 retrieved MAIAC EPIC SSA_{443} remains comparable to OMAERUV SSA_{440} retrievals ($rmse$ of
507 0.04 and $EE_{0.03}\%$ of 57.5% over North America; $rmse$ of 0.04 and $EE_{0.03}\%$ of 66.4% over South
508 America and Southern Africa in Jethva et al., 2014) and TropOMAER SSA_{440} retrievals ($rmse$ of
509 0.04 to 0.04; $EE_{0.03}$ of 48 to 51% in Torres et al., 2020). Additionally, it is worth noting that the
510 current AERONET algorithm has a strong spectral smoothness constraint for the imaginary part
511 of refractive indices, resulting in less representation of BrC (Sinyuk et al., 2022; Eck et al., 2023).
512 By employing the relaxed constraint, they found decreased SSA (e.g., more absorbing) with
513 smaller sky radiance error from wildfire cases containing a large amount of BrC. However for the
514 biomass burning cases shown in Sinyuk et al. (2022) for both North America wildfire smoke and
515 savanna burning smoke in Zambia the difference in spectral SSA at 443 nm were ~ 0.01 or less for
516 the relaxed versus standard V3 constraints, while some differences in SSA at 675 nm were ~ 0.02
517 for North American smoke only. With this update from the AERONET side, we anticipate a



518 potentially better agreement between EPIC and AERONET for SSA₄₄₃ and possibly better for
 519 SSA₆₈₀ in the future.

520 SSA₆₈₀ retrievals from North America show better agreement with AERONET than SSA₄₄₃
 521 with a smaller *MBE* of -0.002 , *rmse* of 0.02, and higher *EE*_{0.03%} (79.8%). However, Central Africa
 522 shows slightly less agreement in SSA₆₈₀ compared to SSA₄₄₃, with a higher positive bias (*MBE* of
 523 0.03) and smaller *EE*_{0.03%} of 60.2%. Additionally, the retrieved range of SSA₆₈₀ is relatively
 524 narrower (~ 0.87 to 0.92) than that of AERONET (~ 0.80 to 0.99). Regardless, the statistics metrics
 525 are much closer to POLDER GRASP SSA₆₈₀ retrievals (*rmse* of 0.06; *MBE* of -0.04 to -0.02 in
 526 Chen et al., 2020).

527 The comparison of EPIC ALH with CALIOP also reveals strong regional dependence.
 528 Most collocated ALH retrievals are relatively high over North America (3-4 km) and sometimes
 529 reach 6-7 km. In Central Africa, ALH ranges from 0 to 4-5 km, with most collocated retrievals
 530 falling within 1-3 km. The *rmse* value is closely related to the range of ALH; thus, it is relatively
 531 high in North America (1.32 km). More favorable validation statistics were extracted from Central
 532 Africa (*rmse* of 0.84 km; *EE*_{0.5km} of 49.4 %; *MBE* of -0.28 km). This level of accuracy, derived
 533 from long-term validation rather than selected individual cases, is better than the operational
 534 TROPOMI ALH (*MBE* of -2.41 to -1.03 km and *rmse* of 1.97-3.56 km in Nanda et al., 2020).
 535

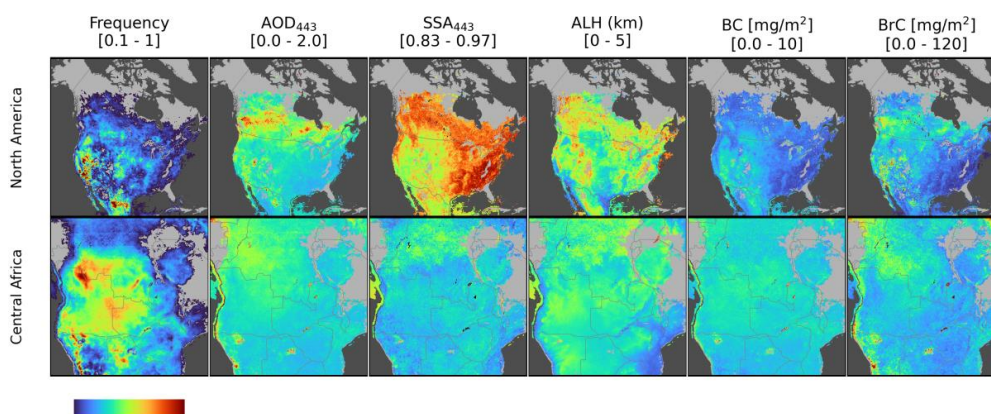


536
 537 Figure 8. Comparison of EPIC smoke AOD₄₄₃ (first column), SSA₄₄₃ (second column), SSA₆₈₀
 538 (third column) with AERONET, and ALH with CALIOP (fourth column). Color represents the
 539 relative frequency of retrievals. The gray dashed lines and shaded areas are the 1:1 reference line
 540 and ranges of expected error: $\pm (0.05 + 0.2 \times \text{AERONET AOD})$; $\pm (\text{AERONET SSA} + 0.03)$ or \pm
 541 $(\text{AERONET SSA} + 0.05)$; and $\pm (\text{CALIOP ALH} + 0.5 \text{ km})$ or $\pm (\text{CALIOP ALH} + 1.0 \text{ km})$.

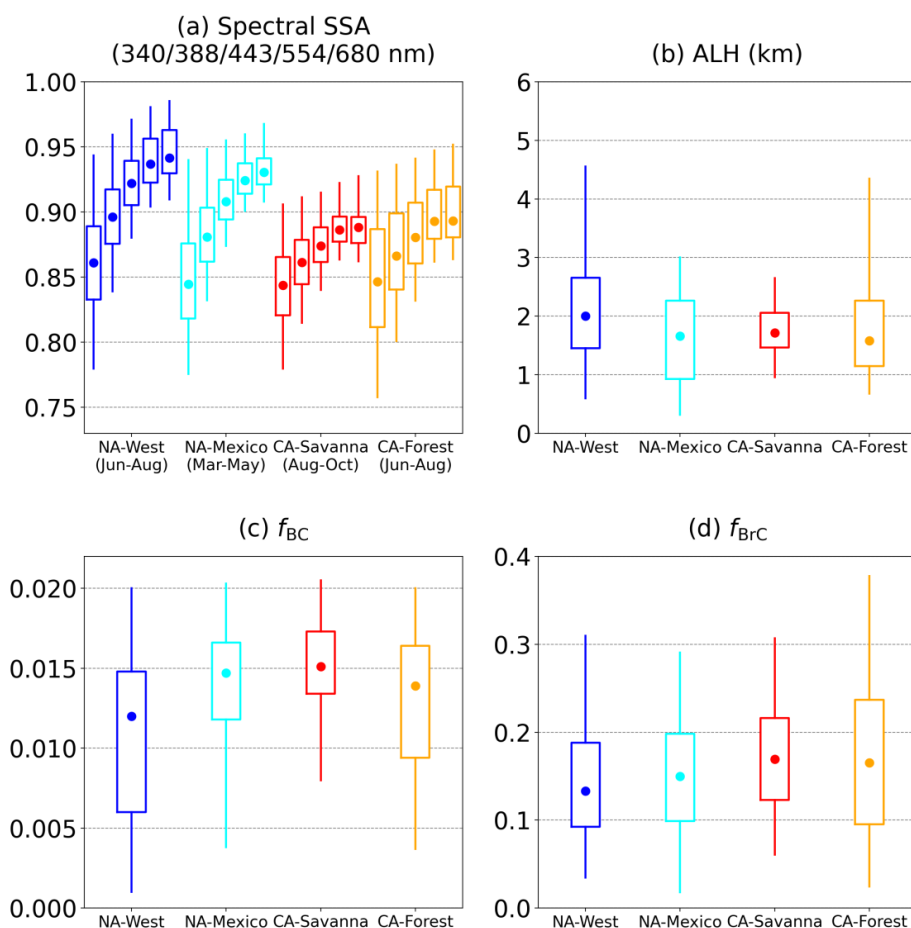


542 3.3 Regional climatology of smoke properties

543 We compiled all the smoke properties retrieved for 2018 and conducted a regional analysis
544 to understand their climatology and relationships with environmental factors such as vegetation
545 and fuel type, as well as meteorological conditions. Regional geographical distributions are
546 illustrated in Fig 9, and the corresponding statistical distributions are presented as box-whisker
547 plots in Fig 10. Regional- and monthly-averaged BC and BrC mass concentrations are presented
548 in Fig 11.
549



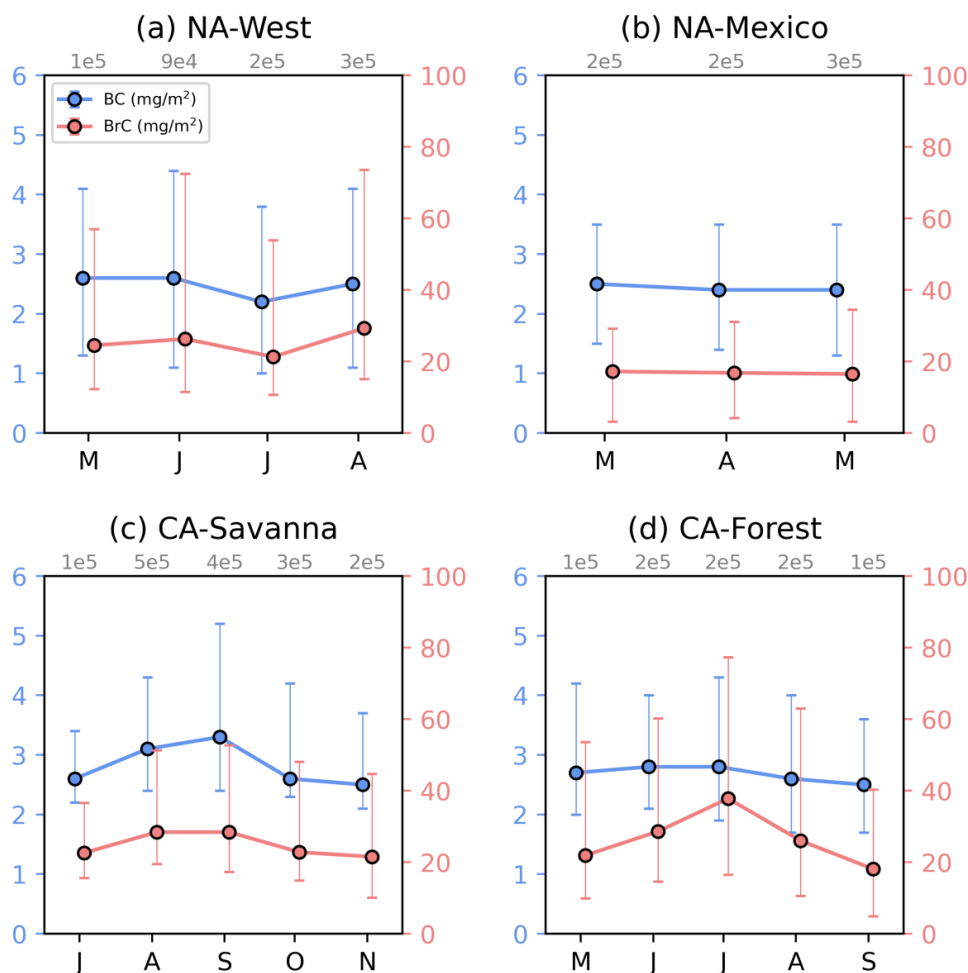
550
551 Figure 9. Spatial distribution of relative retrieval frequency (i.e., relative number of retrievals) and
552 smoke properties (AOD_{443} , SSA_{443} , ALH, and BC and BrC mass concentrations) for 2018 over
553 North America (top panels) and Central Africa (bottom panels). Pixels with retrieval frequencies
554 lower than 10% compared to the regional maximum are filtered out. The color bar scale is indicated
555 at the top of each panel.



556

557 Figure 10. Distribution of (a) spectral SSA, (b) ALH, (c) BC volume fraction, and (d) BrC volume
 558 fraction over western North America (“NA-West”) and Mexico (“NA-Mexico”) in North America,
 559 and savanna (“CA-Savanna”) and tropical forest (“CA-Forest”) in Central Africa. Whiskers give
 560 the 5th and 95th percentiles; boxes represent the 25 and 75th percentiles; and dots denote the 50th
 561 percentile. In (a), five consecutive box-whisker plots for each region represent different
 562 wavelengths (340, 388, 443, 554, and 680 nm from left to right).

563



564
 565 Figure 11. Regional monthly BC and BrC mass concentrations over western North America (“NA-
 566 West”) and Mexico (“NA-Mexico”) in North America, and savanna (“CA-Savanna”) and tropical
 567 forest (“CA-Forest”) regions in Central Africa. Whiskers denote the 15.9th and 84.1st percentiles;
 568 dots denote the 50th percentile. The number of smoke retrievals is displayed in grey at the top of
 569 each panel.

570
 571 Active wildfires occur in late spring and summer over western North America, with
 572 expanded burned areas over the years (Dennison et al., 2014; Kalashnikova et al., 2018; Liu et al.,
 573 2010). Most smoke retrievals were detected over the western United States (e.g., California,
 574 Oregon, Washington) and western Canada (e.g., British Columbia) (Fig 9). The optical properties
 575 were quite distinct between source regions and downwind regions. The western US and western



576 Canada source regions show relatively low SSA and ALH, while central Canada, which is a source
577 region, but also mostly downwind regions for transported heavy smoke plume from western
578 regions, show higher SSA and ALH. This difference is closely related to the smoke aging process
579 discussed in Sec 3.1.1. Spatiotemporally integrated spectral SSA over western North America
580 (“NA-West” region in Fig 2) of 0.86, 0.89, 0.92, 0.94, and 0.95 at 340, 388, 443, 554, and 680 nm,
581 respectively, align with the range 0.915-0.935 at 443 nm and 0.95-0.97 at 680 nm derived from
582 multiple AREONET measurements in September 2020 (Eck et al., 2023). The mean and standard
583 deviation of ALH was 2.2 ± 1.2 km with a wide range of values up to 4.6 km at the 95th percentile
584 (Fig 10b). The mean BC volume fraction of 0.011 ± 0.006 was the lowest among the selected
585 regions. The number of smoke pixels was maximum in August, with the highest BrC mass
586 concentration (median value of 29 mg/m^2), synchronized with seasonal wildfire activities over
587 western North America. Although BC and BrC concentrations can reach up to more than 5 mg/m^2
588 and 100 mg/m^2 , respectively, over some specific regions (Fig 9), the averaged values were not as
589 high due to high spatiotemporal variation (Fig 11a). Another smoke-dominated region in North
590 America is found over Mexico (“NA-Mexico” region in Fig 2), where both natural wildfires and
591 agricultural burns occur annually during the hot and dry season (March to May; Rios et al., 2023).
592 This region exhibited smoke properties with more absorption and lower ALH with lower variation
593 (1.6 ± 0.9 km) than western US.

594 Central Africa is climatologically the largest global biomass burning source, peaking
595 during the austral winter. The region contributes approximately one-third of Earth’s biomass
596 burning emissions from various sources, including wildfires, agricultural fires, and industrial
597 activities (van der Werf et al., 2010). The distribution of smoke retrievals appears relatively
598 homogeneous and similar to that of detected fires, with widespread retrieval frequency in Angola,
599 Democratic Republic of the Congo, and Zambia, and more varied sources in Namibia (Fig 9).
600 During the August–October burning season in Central Africa, aerosol light-absorption is
601 predominantly attributed to BC, a byproduct of savanna burning characterized by significant
602 flaming-phase combustion (Ward et al., 1996). Although the retrieved smoke AOD is not as high
603 as in North America, light absorption over savanna region in Central Africa (“CA-Savanna” region
604 in Fig 2) was more substantial, leading to higher BC and BrC mass concentrations. Low SSA
605 spanned from UV through the visible (0.84, 0.86, 0.88, 0.89, and 0.89 at 340, 388, 443, 554, and
606 680 nm, respectively), with higher BC and BrC volume fractions of 0.015 and 0.178, respectively.
607 The ALH is lower and less variance (1.8 ± 0.6 km; 2.6 km for the 95th percentile) that of western
608 North America. The BC and BrC mass concentrations increased from July, peaked in September
609 (median values of 3.3 mg/m^2 and 28.4 mg/m^2 , respectively), and declined toward November (Fig
610 11c); this aligns with long-term AERONET AOD measurements (Eck et al., 2003) and with
611 AERONET-based BC and BrC estimations (Schuster et al., 2016). By contrast, smoke from
612 tropical forest fires in Central Africa (“CA-Forest” region in Fig 2) shows slightly less absorption
613 with lower BC volume fraction (0.013) and larger variabilities of BrC volume fraction ($0.018 \pm$
614 0.11) and ALH (1.9 ± 1.1 km) than that of savanna region. BC and BrC mass concentrations over



615 the tropical forest region in Central Africa peak in July (earlier than savanna region) with lower
616 BC (2.8 mg/m^2) and higher BrC (37.8 mg/m^2 ; Fig 11d) than those of the savanna region.

617 4. Discussions

618 4.1 Comparison of the BrC to BC mass concentration ratio with other studies

619 The ratio between OC and EC (OC/EC) is widely used to elucidate the apportionment of
620 carbonaceous components in smoke particles as a proxy for assessing the dominance of primary
621 emissions from flaming combustion (e.g., fossil fuel) versus smoldering combustion emissions
622 and secondary formation of OC (e.g., biomass burning, wildfires, secondary organic aerosol (SOA)
623 formation) (Lim and Turpin, 2002; Pokhrel et al., 2016). As BrC is an absorbing OC among total
624 OC, we inferred regional BrC-to-BC column mass concentration ratios (BrC/BC) from EPIC and
625 compared them with those from other studies providing BrC/BC or OC/EC.

626 Results of BrC/BC ratio from this study in North America and Central Africa are compared
627 with other previous studies in Fig 12. The absolute BC and BrC volume fractions in Central Africa
628 were higher than in North America, resulting in similar median values of the BrC/BC mass
629 concentration ratio (7.3 for North America and 8.0 for Central Africa). When the ratios are
630 categorized into different AOD ranges, the BrC/BC increases with AOD from both regions. For
631 two groups of $\text{AOD} < 0.6$ (“low-moderate AOD”) and $0.6 < \text{AOD} < 2.0$ (“high AOD”), the median
632 BrC/BC is higher in Central Africa (7.2 and 10.1) than in North America (6.9 and 8.9). The
633 variance, represented as the range of estimations, is more significant in North America for the two
634 groups, which could be ascribed to more diverse fuel types from natural, residential, and
635 agricultural sources and related emission processes (Xiong et al., 2022). For the cases of $\text{AOD} >$
636 2.0 (“extremely high AOD”), which corresponds to 2.6% and 0.7% of the entire retrieval record
637 in North America and Central Africa, respectively, North America showed a higher BrC/BC ratio
638 (median value of 41.5) with a higher variance than Central Africa (median value of 17.7). This
639 higher BrC/BC ratio in North America, compared to Central Africa, may have its origin in more
640 common smoldering combustion and/or more SOA formation during transport. Most “extremely
641 high AOD” cases were observed from transport plumes, where the increased BrC/BC ratio is
642 associated with their aging processes including SOA formation. These results are consistent with
643 POLDER/GRASP and MISR aerosol components analysis (Li et al., 2022; Junghenn Noyes et al.,
644 2022).

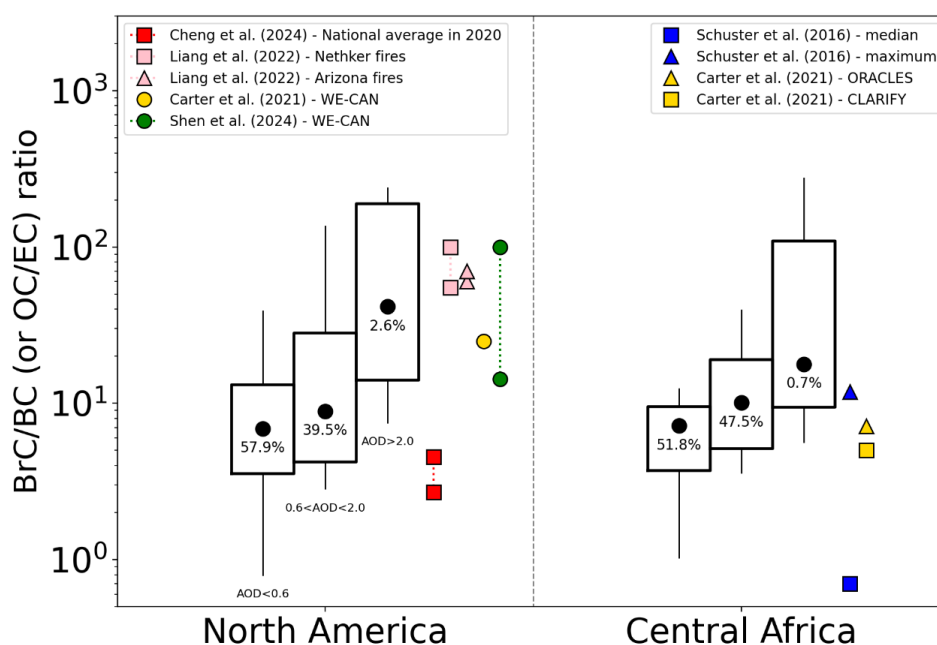
645 Our estimates exhibit relatively high variance because they encompassed all pixels detected
646 as smoke in the retrieval algorithm over the continents in 2018, rather than being limited to selected
647 heavy plumes. The national average of OC/EC ratio (3.6 ± 0.9) obtained from U.S. EPA ground-
648 based chemical composition measurement networks (including CSN and IMPROVE) for all
649 sources, not only for smoke sources, (Cheng et al., 2024) falls within the estimates from EPIC’s
650 “low-moderate AOD” group. OC/EC ratios obtained from specific wildfire samples including WE-
651 CAN campaign during 2018 July-September over western US (Liang et al., 2022; Carter et al.,
652 2021) range from approximately 14 to 100, corresponding to the “extremely high AOD” group. It



653 is important to note that although the BrC/BC ratio is smaller than the OC/EC ratio, obtaining an
 654 accurate BrC/BC is challenging without proper measurements separating BrC from OC, which is
 655 rarely done in experiments.

656 The ORACLES (August–September 2016) and CLARIFY (August 2017) campaigns over
 657 the eastern South Atlantic Ocean (Carter et al., 2021) measured transported smoke aerosols from
 658 Central Africa. The general level of AOD at 550 nm for both campaigns was ~0.3 to ~0.7
 659 (Haywood et al., 2021; Sayer et al., 2019), and corresponding OC/EC ratios were 5-7, which are
 660 consistent with the estimated EPIC ranges for “low-moderate AOD” and “high AOD”. Another
 661 comparison can be made with the BrC/BC mass concentration ratio inferred from AERONET
 662 measurements (Schuster et al., 2016). Although the definition is similar to ours, both using
 663 column-integrated and remote-sensing-based values, it shows relatively lower values than ours.
 664 This difference could be attributable to the different wavelengths (i.e., UV-Vis for EPIC, Vis-NIR
 665 for AERONET) used for the measurements and different assumptions in the components (e.g.,
 666 dependence of composition on particle size in Schuster et al., 2016).

667 The EPIC BrC/BC ratios increased with AOD, representing aging processes during
 668 transport over North America and Central Africa. They are generally consistent with other studies
 669 despite different measurement characteristics, such as OC/EC vs. BrC/BC, and *in-situ* versus
 670 remote sensing.



671



672 Fig 12. Regional EPIC-derived BrC to BC column mass concentration ratios across three AOD
673 ranges (AOD < 0.6, 0.6 < AOD < 2.0, and AOD > 2.0). Each box-whisker plot comprises the 5th,
674 15.9th, 50th, 84.1st, and 95th percentiles. The percentages of retrievals per each AOD range are
675 denoted within the box. On the right side of each region panel, the values (or range) of the BrC-
676 to-BC ratio (only for Schuster et al., 2016) or OC-to-BC ratio (all others) from other studies are
677 shown.

678 4.2 Uncertainty of volume fractions due to assumed BC and BrC refractive indices

679 Assumed spectral imaginary refractive indices of BC and BrC determine their inferred
680 volume fractions. Identical spectral absorption can result in lower BC and BrC fractions with
681 higher BC and BrC imaginary refractive indices and vice versa. As most satellite measurements,
682 including EPIC, lack sensitivity to infer both the imaginary refractive indices of inclusions and
683 their volume fractions, we must assume the imaginary refractive indices of inclusions to infer their
684 volume fractions. Here, we investigate the effect of this assumption on the inferred volume
685 fractions and assess the resulting uncertainties.

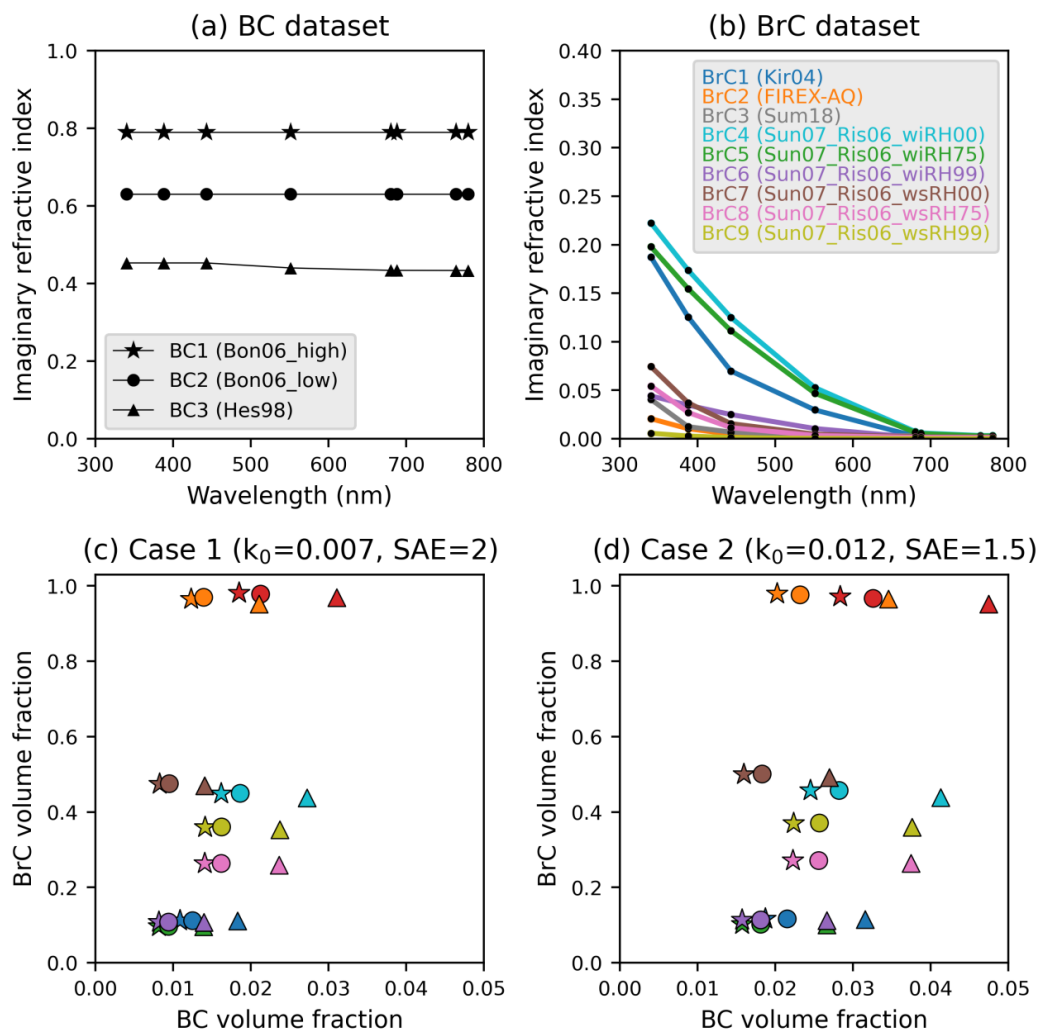
686 A total of three different BC datasets were considered (Fig 13a). “BC1”, which we used,
687 and “BC2” were derived from multiple measurements combined with the assumption that light-
688 absorbing carbon has a single refractive index and that variation can be expressed by the
689 Bruggeman effective-medium theory (Bond and Bergstrom, 2006). “BC3”, utilized in aerosol
690 modeling for AirMSPI analysis (Kalashnikova et al., 2018), was originally referred to as the “soot”
691 component of the Optical Properties of Aerosols and Clouds (OPAC) dataset described in Hess et
692 al. (1998). The value of k is between 0.4 and 0.8 and is spectrally invariant or nearly invariant.

693 We tested nine different BrC datasets (Fig 13b). “BrC1”, which we used, was derived from
694 organic carbon extracted from wood burning and SAFARI biomass smoke samples as described
695 in Kirchstetter et al. (2004). “BrC2” is an Air-MSPI retrieved value during the FIREX-AQ
696 campaign (O. Kalashnikova, personal communication, May 19, 2020). “BrC3” represents aerosols
697 emitted from the smoldering combustion of Boreal and Indonesian peatlands (Sumlin et al., 2018).
698 “BrC4”, “BrC5”, and “BrC6” represent water-insoluble BrC with relative humidity of 0%, 75%,
699 and 99%, respectively, calculated by combining the upper curve of Sun et al. (2007) and
700 hygroscopic properties in Rissler et al. (2006). “BrC7”, “BrC8”, and “BrC9” are the same but
701 represent water-soluble BrC. These datasets were obtained from the Table of Aerosol Optics (TAO)
702 dataset within the framework of the Models, In situ, and Remote sensing of Aerosols (MIRA)
703 working group projects (<https://science.larc.nasa.gov/mira-wg/>).

704 Here, two smoke cases were analyzed: “Case 1” (k_0 of 0.007 and SAE of 2) and “Case 2”
705 (k_0 of 0.012 and SAE of 1.5), representing the most populated EPIC retrievals in the AERONET
706 validation over North America and Central Africa, respectively. For Case 1, the f_{BC} and f_{BrC} based
707 on our current assumptions are 0.011 and 0.112, respectively (marked with a “star” marker in dark
708 blue in Fig 13c). With different assumptions for inclusion properties, they have a range of 0.008-
709 0.031 and 0.096-0.982, respectively. Less absorbing BC assumptions (i.e., smaller k) result in
710 increased f_{BC} to 0.012 (“BC2” and “BrC1”) and 0.018 (“BC3” and “BrC2”). The maximum



711 difference of f_{BrC} is 0.013, with the lowest absorption in BrC (“BrC9”). The potential f_{BrC} values
712 exhibit greater variability. The f_{BrC} value with the current assumption (0.112) is one of the lowest
713 values among tested combinations and similar to those from “BrC2” and “BrC3”, which have
714 stronger absorption than others. The BrC assumptions with less absorbing properties show higher
715 f_{BrC} from 0.264 to 0.981. We also tested the spectral k for dark BrC obtained from the FIREX-AQ
716 campaign in the western US (Chakrabarty et al., 2023). They showed an estimated f_{BrC} close to
717 zero because of the relatively high k of 0.1 at 680 nm. Case 2 is converted to higher f_{BrC} (0.019)
718 and similar f_{BrC} (0.117) compared to Case 1 with the default assumption. The range of f_{BrC} and
719 f_{BrC} from the different combinations is 0.016-0.047 and 0.101-0.980, respectively. It is essential
720 to acknowledge that inferring volume fractions and mass concentrations is based on assumed
721 inclusion properties, introducing some uncertainties. The assumed properties of BC and BrC will
722 need to be refined in future studies (e.g., a suggested concept in Kahn et al., 2017) to enhance the
723 accuracy of our findings.
724



725

726 Fig 13. Spectral imaginary refractive indices of (a) BC and (b) BrC. Range of BC and BrC volume
 727 fractions for (c) “Case 1” (k_0 of 0.007 and SAE of 2) and (d) “Case 2” (k_0 of 0.012 and SAE of
 728 1.5). The star, circle, and triangle symbols in (c) and (d) refer to different BC assumptions of
 729 “BC1”, “BC2”, and “BC3” in (a). The different colors in (c) and (d) refer to different BrC
 730 assumptions from “BrC1” to “BrC9” in (b).

731 **5. Summary and conclusions**

732 This study introduced a technique inferring the BC and BrC light-absorbing components
 733 of smoke aerosol by leveraging the spectral absorption retrieved in the MAIAC EPIC algorithm.
 734 Spectral absorption retrievals allowed us to quantify the BC and BrC fractions, which were then



735 converted to column-integrated mass concentrations assuming the particle mass extinction
736 efficiency. We assumed that BC and BrC are internally mixed with a non-absorbing host
737 representing non-absorbing OC, sulfate, nitrate, or ammonium components, using the Maxwell
738 Garnett effective medium approximation.

739 We analyzed regional characteristics over North America and Central Africa in 2018,
740 utilizing all available MAIAC EPIC smoke property retrievals (AOD, spectral SSA, ALH, and BC
741 and BrC volume fractions and mass concentrations). Selected cases showed that smoke aerosols
742 emitted from wildfires over western North America exhibited extremely high AOD up to ~6 with
743 elevated ALH (6-7 km). Dynamic changes in spectral absorption and significant BrC components
744 were observed during continental-scale transport. The EPIC MAIAC products successfully
745 monitored the transport and evolution of smoke optical properties with high temporal resolution
746 during regional-to-continental-scale transport. Biomass-burning smoke over Central Africa
747 displayed higher absorption with greater BC and BrC fractions than North America, showing
748 seasonal changes in major source locations. They also showed less strong zonal transport with
749 ALH closer to the surface, and diurnal change in smoke amounts related to fire activities.

750 EPIC-retrieved AOD₄₄₃, SSA₄₄₃, SSA₆₈₀, and ALH agreed with collocated AERONET and
751 CALIOP measurements with *rmse* of 0.2, 0.03-0.04, 0.02-0.04, and 0.8-1.3 km, respectively, and
752 the overall accuracies were comparable to other operational satellite products such as OMI,
753 TROPOMI, and POLDER. Spatiotemporally integration of measurements revealed geographical
754 characteristics and distinct differences in optical properties, ALH, and inferred BC and BrC,
755 closely linked to burning types and meteorological conditions. Smoke from forest fires in western
756 North America shows SSA₄₄₃ of 0.92 with low BC volume fraction of 0.011 and high ALH with
757 larger standard deviation (2.2 ± 1.2 km). The wildfires and agricultural fires over the Mexico
758 region generated smoke with more absorption and lower ALH. The Savanna region in Central
759 Africa during August to October shows smoke properties with most absorbing with high BC and
760 BrC volume fractions (0.015 and 0.178, respectively) and lower ALH with smaller variation.
761 Smoke from tropical forests in Central Africa exhibits absorption between that of western US and
762 savanna regions and high ALH variability. The impact of assumed imaginary refractive indices of
763 BC and BrC in estimating their volume fractions was analyzed based on a literature survey,
764 presenting the corresponding uncertainty ranges of our retrievals.

765 Although we focused on North America and Central Africa, smoke aerosols have a
766 significant impact on air quality and climate globally. Future studies will extend the analysis to
767 other regions using almost a decade of EPIC measurements since 2015, with extensive validation
768 and error analysis using multiple measurements, including AERONET, CALIOP, and in-situ
769 aerosol composition data.

770 The MAIAC EPIC smoke aerosol components presented here could serve as valuable *a*
771 *priori* information for recent and upcoming satellite missions such as the Plankton, Aerosol, Cloud,
772 ocean Ecosystem (PACE; <https://pace.gsfc.nasa.gov/>) (Remer et al., 2019a, b), the Multi-Angle
773 Imager for Aerosols (MAIA; <https://maia.jpl.nasa.gov/>) (Diner et al., 2018), EPS-SG Multi-
774 Viewing Multi-Channel Multi-Polarisation Imaging (3MI) (Fougnie et al., 2018) and Atmosphere



775 Observing System (AOS; <https://aos.gsfc.nasa.gov/>), focusing on retrieving aerosol microphysical
776 and optical properties, and inferring chemical composition, with higher accuracy from multi-angle
777 polarization measurements. Integration of our results with other in-situ and remote sensing
778 measurements and models (e.g., Kahn et al., 2023) should enhance our understanding of smoke
779 aerosol aging processes, improve air quality monitoring and forecasting, and refine the
780 quantification of radiative forcing due to smoke aerosols on a global scale.

781 **Author contributions**

782 M. Choi and AL designed the study with discussions with GLS and SG. GLS provided
783 major guidance on developing the BC and BrC estimation algorithms. AL and WY provided the
784 MAIAC EPIC products. AL and SK conducted RT calculations (LUTs for MAIAC). M. Choi, AL,
785 YW and SG developed the code and performed the retrievals. GLS and OK participated in the
786 collection of refractive indices data. M. Choi, AL, GLS, and SG analyzed the results. M. Choi and
787 AL wrote the manuscript with comments from all co-authors.

788 **Competing interests**

789 The authors declare that they have no conflict of interest.

790 **Data availability**

791 The retrievals can be requested directly from the corresponding author
792 (myungje.choi@nasa.gov or alexei.i.lyapustin@nasa.gov).

793 **Acknowledgment**

794 The work of A. Lyapustin, M. Choi, S. Go, and Y. Wang was funded by the NASA
795 DSCOVR program (21-DSCOVR-21-0004; manager Dr. R. Eckman) and in part by the NASA
796 PACE program (19-PACESAT19-0039). J. S Reid was funded by the Office of Naval Research,
797 Code 322. The work of H. Moosmüller was supported in part by the National Science Foundation
798 under Grant No. OIA- 2148788 and by NASA under grant 80NSSC20M0205 (PACE SAT Project:
799 PACE UV ROAD). We are grateful to the AERONET team for providing validation data and to
800 the NASA Center for Climate Simulations providing resources for the EPIC data processing.

801 **References**

802 Ahn, C., Torres, O., Jethva, H., Tiruchirapalli, R., and Huang, L.-K.: Evaluation of Aerosol
803 Properties Observed by DSCOVR/EPIC Instrument From the Earth-Sun Lagrange 1 Orbit, *J.*
804 *Geophys. Res. Atmos.*, 126, e2020JD033651,
805 <https://doi.org/https://doi.org/10.1029/2020JD033651>, 2021.
806 Andreae, M. O.: Emission of trace gases and aerosols from biomass burning – an updated



- 807 assessment, *Atmos. Chem. Phys.*, 19, 8523–8546, <https://doi.org/10.5194/acp-19-8523-2019>,
808 2019.
- 809 Andreae, M. O. and Gelencsér, A.: Black carbon or brown carbon? the nature of light-absorbing
810 carbonaceous aerosols, *Atmos. Chem. Phys.*, 6, 3131–3148, <https://doi.org/10.5194/acp-6-3131-2006>, 2006.
- 812 Andreae, M. O. and Merlet, P.: Emission of trace gases and aerosols from biomass burning, *Global
813 Biogeochem. Cycles*, 15, 955–966, <https://doi.org/10.1029/2000GB001382>, 2001.
- 814 Bellouin, N., Boucher, O., Haywood, J., and Reddy, M. S.: Global estimate of aerosol direct
815 radiative forcing from satellite measurements, *Nature*, 438, 1138–1141,
816 <https://doi.org/10.1038/nature04348>, 2005.
- 817 Bhandari, J., China, S., Chandrakar, K. K., Kinney, G., Cantrell, W., Shaw, R. A., Mazzoleni, L.
818 R., Giroto, G., Sharma, N., Gorkowski, K., Gilardoni, S., Decesari, S., Facchini, M. C., Zanca,
819 N., Pavese, G., Esposito, F., Dubey, M. K., Aiken, A. C., Chakrabarty, R. K., Moosmüller,
820 H., Onasch, T. B., Zaveri, R. A., Scarnato, B. V., Fialho, P., and Mazzoleni, C.: Extensive
821 Soot Compaction by Cloud Processing from Laboratory and Field Observations, *Sci. Rep.*, 9,
822 <https://doi.org/10.1038/s41598-019-48143-y>, 2019.
- 823 Bohren, C. F. and Huffman, D. R.: *Absorption and Scattering of Light by Small Particles*, Wiley,
824 <https://doi.org/10.1002/9783527618156>, 1998.
- 825 Bond, T. C. and Bergstrom, R. W.: *Light Absorption by Carbonaceous Particles: An Investigative
826 Review*, *Aerosol Sci. Technol.*, 40, 27–67, <https://doi.org/10.1080/02786820500421521>,
827 2006.
- 828 Bond, T. C., Doherty, S. J., Fahey, D. W., Forster, P. M., Berntsen, T., Deangelo, B. J., Flanner,
829 M. G., Ghan, S., Kärcher, B., Koch, D., Kinne, S., Kondo, Y., Quinn, P. K., Sarofim, M. C.,
830 Schultz, M. G., Schulz, M., Venkataraman, C., Zhang, H., Zhang, S., Bellouin, N., Guttikunda,
831 S. K., Hopke, P. K., Jacobson, M. Z., Kaiser, J. W., Klimont, Z., Lohmann, U., Schwarz, J.
832 P., Shindell, D., Storelvmo, T., Warren, S. G., and Zender, C. S.: Bounding the role of black
833 carbon in the climate system: A scientific assessment, *J. Geophys. Res. Atmos.*, 118, 5380–
834 5552, <https://doi.org/10.1002/jgrd.50171>, 2013.
- 835 Bond, W. J. and Keeley, J. E.: Fire as a global “herbivore”: the ecology and evolution of flammable
836 ecosystems., *Trends Ecol. Evol.*, 20, 387–94, <https://doi.org/10.1016/j.tree.2005.04.025>,
837 2005.
- 838 Carter, T. S., Heald, C. L., Cappa, C. D., Kroll, J. H., Campos, T. L., Coe, H., Cotterell, M. I.,
839 Davies, N. W., Farmer, D. K., Fox, C., Garofalo, L. A., Hu, L., Langridge, J. M., Levin, E. J.
840 T., Murphy, S. M., Pokhrel, R. P., Shen, Y., Szpek, K., Taylor, J. W., and Wu, H.:
841 Investigating Carbonaceous Aerosol and Its Absorption Properties From Fires in the Western
842 United States (WE-CAN) and Southern Africa (ORACLES and CLARIFY), *J. Geophys. Res.
843 Atmos.*, 126, 647–650, <https://doi.org/10.1029/2021JD034984>, 2021.
- 844 Chakrabarty, R. K., Moosmüller, H., Chen, L.-W. A., Lewis, K., Arnott, W. P., Mazzoleni, C.,
845 Dubey, M. K., Wold, C. E., Hao, W. M., and Kreidenweis, S. M.: Brown carbon in tar balls
846 from smoldering biomass combustion, *Atmos. Chem. Phys.*, 10, 6363–6370,
847 <https://doi.org/10.5194/acp-10-6363-2010>, 2010.
- 848 Chakrabarty, R. K., Shetty, N. J., Thind, A. S., Beeler, P., Sumlin, B. J., Zhang, C., Liu, P., Idrobo,
849 J. C., Adachi, K., Wagner, N. L., Schwarz, J. P., Ahern, A., Sedlacek, A. J., Lambe, A., Daube,
850 C., Lyu, M., Liu, C., Herndon, S., Onasch, T. B., and Mishra, R.: Shortwave absorption by
851 wildfire smoke dominated by dark brown carbon, *Nat. Geosci.*,
852 <https://doi.org/10.1038/s41561-023-01237-9>, 2023.



- 853 Chen, C., Dubovik, O., Fuertes, D., Litvinov, P., Lapyonok, T., Lopatin, A., Ducos, F., Derimian,
854 Y., Herman, M., Tanré, D., Remer, L. A., Lyapustin, A., Sayer, A. M., Levy, R. C., Christina
855 Hsu, N., Descloitres, J., Li, L., Torres, B., Karol, Y., Herrera, M., Herreras, M., Aspetsberger,
856 M., Wanzenboeck, M., Bindreiter, L., Marth, D., Hangler, A., and Federspiel, C.: Validation
857 of GRASP algorithm product from POLDER/PARASOL data and assessment of multi-
858 angular polarimetry potential for aerosol monitoring, *Earth Syst. Sci. Data*, 12, 3573–3620,
859 <https://doi.org/10.5194/essd-12-3573-2020>, 2020.
- 860 Cheng, B., Alapaty, K., and Arunachalam, S.: Spatiotemporal trends in PM_{2.5} chemical
861 composition in the conterminous U.S. during 2006–2020, *Atmos. Environ.*, 316, 120188,
862 <https://doi.org/10.1016/j.atmosenv.2023.120188>, 2024.
- 863 Choi, Y., Ghim, Y. S., Zhang, Y., Park, S. M., and Song, I. H.: Estimation of surface concentrations
864 of black carbon from long-term measurements at aeronet sites over korea, *Remote Sens.*, 12,
865 1–24, <https://doi.org/10.3390/rs12233904>, 2020.
- 866 Corbin, J. C., Modini, R. L., and Gysel-Beer, M.: Mechanisms of soot-aggregate restructuring and
867 compaction, *Aerosol Sci. Technol.*, 57, 89–111,
868 <https://doi.org/10.1080/02786826.2022.2137385>, 2023.
- 869 Dennison, P. E., Brewer, S. C., Arnold, J. D., and Moritz, M. A.: Large wildfire trends in the
870 western United States, 1984–2011, *Geophys. Res. Lett.*, 41, 2928–2933,
871 <https://doi.org/10.1002/2014GL059576>, 2014.
- 872 Diner, D. J., Boland, S. W., Brauer, M., Bruegge, C., Burke, K. A., Chipman, R., Di Girolamo, L.,
873 Garay, M. J., Hasheminassab, S., and Hyer, E.: Advances in multiangle satellite remote
874 sensing of speciated airborne particulate matter and association with adverse health effects:
875 from MISR to MAIA, *J. Appl. Remote Sens.*, 12, 1, <https://doi.org/10.1117/1.JRS.12.042603>,
876 2018.
- 877 Dubovik, O. and King, M. D.: A flexible inversion algorithm for retrieval of aerosol optical
878 properties from Sun and sky radiance measurements, *J. Geophys. Res. Atmos.*, 105, 20673–
879 20696, <https://doi.org/10.1029/2000JD900282>, 2000.
- 880 Dubovik, O., Holben, B., Eck, T. F., Smirnov, A., Kaufman, Y. J., King, M. D., Tanré, D., and
881 Slutsker, I.: Variability of Absorption and Optical Properties of Key Aerosol Types Observed
882 in Worldwide Locations, *J. Atmos. Sci.*, 59, 590–608, [https://doi.org/10.1175/1520-0469\(2002\)059<0590:VOAOP>2.0.CO;2](https://doi.org/10.1175/1520-0469(2002)059<0590:VOAOP>2.0.CO;2), 2002.
- 884 Dubovik, O., Sinyuk, A., Lapyonok, T., Holben, B. N., Mishchenko, M., Yang, P., Eck, T. F.,
885 Volten, H., Muñoz, O., Veihelmann, B., van der Zande, W. J., Leon, J. F., Sorokin, M., and
886 Slutsker, I.: Application of spheroid models to account for aerosol particle nonsphericity in
887 remote sensing of desert dust, *J. Geophys. Res. Atmos.*, 111, 1–34,
888 <https://doi.org/10.1029/2005JD006619>, 2006.
- 889 Dubovik, O., Herman, M., Holdak, A., Lapyonok, T., Tanré, D., Deuzé, J. L., Ducos, F., Sinyuk,
890 A., and Lopatin, A.: Statistically optimized inversion algorithm for enhanced retrieval of
891 aerosol properties from spectral multi-angle polarimetric satellite observations, *Atmos. Meas.
892 Tech.*, 4, 975–1018, <https://doi.org/10.5194/amt-4-975-2011>, 2011.
- 893 Dubovik, O., Lapyonok, T., Litvinov, P., Herman, M., Fuertes, D., Ducos, F., Torres, B., Derimian,
894 Y., Huang, X., Lopatin, A., Chaikovskiy, A., Aspetsberger, M., and Federspiel, C.: GRASP:
895 a versatile algorithm for characterizing the atmosphere, *SPIE Newsroom*,
896 <https://doi.org/10.1117/2.1201408.005558>, 2014.
- 897 Duncan, B. N., Martin, R. V., Staudt, A. C., Yevich, R., and Logan, J. A.: Interannual and seasonal
898 variability of biomass burning emissions constrained by satellite observations, *J. Geophys.*



- 899 Res. Atmos., 108, <https://doi.org/10.1029/2002JD002378>, 2003.
- 900 Eck, T. F., Holben, B. N., Reid, J. S., Dubovik, O., Smirnov, A., O'Neill, N. T., Slutsker, I., and
901 Kinne, S.: Wavelength dependence of the optical depth of biomass burning, urban, and desert
902 dust aerosols, *J. Geophys. Res.*, 104, 31333, <https://doi.org/10.1029/1999JD900923>, 1999.
- 903 Eck, T. F., Holben, B. N., Ward, D. E., Mukelabai, M. M., Dubovik, O., Smirnov, A., Schafer, J.
904 S., Hsu, N. C., Piketh, S. J., Queface, A., Le Roux, J., Swap, R. J., and Slutsker, I.: Variability
905 of biomass burning aerosol optical characteristics in southern Africa during the SAFARI 2000
906 dry season campaign and a comparison of single scattering albedo estimates from radiometric
907 measurements, *J. Geophys. Res. Atmos.*, 108, <https://doi.org/10.1029/2002jd002321>, 2003.
- 908 Eck, T. F., Holben, B. N., Reid, J. S., Mukelabai, M. M., Piketh, S. J., Torres, O., Jethva, H. T.,
909 Hyer, E. J., Ward, D. E., Dubovik, O., Sinyuk, A., Schafer, J. S., Giles, D. M., Sorokin, M.,
910 Smirnov, A., and Slutsker, I.: A seasonal trend of single scattering albedo in southern African
911 biomass-burning particles: Implications for satellite products and estimates of emissions for
912 the world's largest biomass-burning source, *J. Geophys. Res. Atmos.*, 118, 6414–6432,
913 <https://doi.org/10.1002/jgrd.50500>, 2013.
- 914 Eck, T. F., Holben, B. N., Reid, J. S., Sinyuk, A., Giles, D. M., Arola, A., Slutsker, I., Schafer, J.
915 S., Sorokin, M. G., Smirnov, A., LaRosa, A. D., Kraft, J., Reid, E. A., O'Neill, N. T., Welton,
916 E. J., and Menendez, A. R.: The extreme forest fires in California/Oregon in 2020: Aerosol
917 optical and physical properties and comparisons of aged versus fresh smoke, *Atmos. Environ.*,
918 305, <https://doi.org/10.1016/j.atmosenv.2023.119798>, 2023.
- 919 Fougnie, B., Marbach, T., Lacan, A., Lang, R., Schlüssel, P., Poli, G., Munro, R., and Couto, A.
920 B.: The multi-viewing multi-channel multi-polarisation imager – Overview of the 3MI
921 polarimetric mission for aerosol and cloud characterization, *J. Quant. Spectrosc. Radiat.*
922 *Transf.*, 219, 23–32, <https://doi.org/10.1016/j.jqsrt.2018.07.008>, 2018.
- 923 Garnett, J. C. M.: XII. Colours in metal glasses and in metallic films, *Philos. Trans. R. Soc. London.*
924 *Ser. A, Contain. Pap. a Math. or Phys. Character*, 203, 385–420,
925 <https://doi.org/10.1098/rsta.1904.0024>, 1904.
- 926 Giles, D. M., Holben, B. N., Eck, T. F., Sinyuk, A., Smirnov, A., Slutsker, I., Dickerson, R. R.,
927 Thompson, A. M., and Schafer, J. S.: An analysis of AERONET aerosol absorption properties
928 and classifications representative of aerosol source regions, *J. Geophys. Res. Atmos.*, 117, 1–
929 16, <https://doi.org/10.1029/2012JD018127>, 2012.
- 930 Giles, D. M., Sinyuk, A., Sorokin, M. G., Schafer, J. S., Smirnov, A., Slutsker, I., Eck, T. F.,
931 Holben, B. N., Lewis, J. R., Campbell, J. R., Welton, E. J., Korkin, S. V., and Lyapustin, A.
932 I.: Advancements in the Aerosol Robotic Network (AERONET) Version 3 database –
933 automated near-real-time quality control algorithm with improved cloud screening for Sun
934 photometer aerosol optical depth (AOD) measurements, *Atmos. Meas. Tech.*, 12, 169–209,
935 <https://doi.org/10.5194/amt-12-169-2019>, 2019.
- 936 Go, S., Kim, J., Park, S. S., Kim, M., Lim, H., Kim, J. Y., Lee, D. W., and Im, J.: Synergistic use
937 of hyperspectral uv-visible omi and broadband meteorological imager modis data for a
938 merged aerosol product, *Remote Sens.*, 12, 1–34, <https://doi.org/10.3390/rs12233987>, 2020.
- 939 Go, S., Lyapustin, A., Schuster, G. L., Choi, M., Ginoux, P., Chin, M., Kalashnikova, O., Dubovik,
940 O., Kim, J., da Silva, A., Holben, B., and Reid, J. S.: Inferring iron-oxide species content in
941 atmospheric mineral dust from DSCOVER EPIC observations, *Atmos. Chem. Phys.*, 22, 1395–
942 1423, <https://doi.org/10.5194/acp-22-1395-2022>, 2022.
- 943 Gyawali, M., Arnott, W., Zaveri, R., Song, C., Flowers, B., Dubey, M., Setyan, A., Zhang, Q.,
944 China, S., Mazzoleni, C., Gorkowski, K., Subramanian, R., and Moosmüller, H.: Evolution



- 945 of Multispectral Aerosol Absorption Properties in a Biogenically-Influenced Urban
946 Environment during the CARES Campaign, *Atmosphere (Basel)*, 8, 217,
947 <https://doi.org/10.3390/atmos8110217>, 2017.
- 948 Haywood, J. M., Abel, S. J., Barrett, P. A., Bellouin, N., Blyth, A., Bower, K. N., Brooks, M.,
949 Carslaw, K., Che, H., Coe, H., Cotterell, M. I., Crawford, I., Cui, Z., Davies, N., Dingley, B.,
950 Field, P., Formenti, P., Gordon, H., de Graaf, M., Herbert, R., Johnson, B., Jones, A. C.,
951 Langridge, J. M., Malavelle, F., Partridge, D. G., Peers, F., Redemann, J., Stier, P., Szpek, K.,
952 Taylor, J. W., Watson-Parris, D., Wood, R., Wu, H., and Zuidema, P.: The CLOUD–Aerosol–
953 Radiation Interaction and Forcing: Year 2017 (CLARIFY-2017) measurement campaign,
954 *Atmos. Chem. Phys.*, 21, 1049–1084, <https://doi.org/10.5194/acp-21-1049-2021>, 2021.
- 955 Hess, M., Koepke, P., and Schult, I.: Optical Properties of Aerosols and Clouds: The Software
956 Package OPAC, *Bull. Am. Meteorol. Soc.*, 79, 831–844, [https://doi.org/10.1175/1520-0477\(1998\)079<0831:OPOAAC>2.0.CO;2](https://doi.org/10.1175/1520-0477(1998)079<0831:OPOAAC>2.0.CO;2), 1998.
- 958 Hobbs, P. V., Reid, J. S., Kotchenruther, R. A., Ferek, R. J., and Weiss, R.: Direct Radiative
959 Forcing by Smoke from Biomass Burning, *Science (80-.)*, 275, 1777–1778,
960 <https://doi.org/10.1126/science.275.5307.1777>, 1997.
- 961 Hoffer, A., Gelencsér, A., Guyon, P., Kiss, G., Schmid, O., Frank, G. P., Artaxo, P., and Andreae,
962 M. O.: Optical properties of humic-like substances (HULIS) in biomass-burning aerosols,
963 *Atmos. Chem. Phys.*, 6, 3563–3570, <https://doi.org/10.5194/acp-6-3563-2006>, 2006.
- 964 Holben, B. N., Eck, T. F., Slutsker, I., Tanré, D., Buis, J. P., Setzer, A., Vermote, E., Reagan, J.
965 A., Kaufman, Y. J., Nakajima, T., Lavenu, F., Jankowiak, I., and Smirnov, A.: AERONET—
966 A Federated Instrument Network and Data Archive for Aerosol Characterization, *Remote
967 Sens. Environ.*, 66, 1–16, [https://doi.org/10.1016/S0034-4257\(98\)00031-5](https://doi.org/10.1016/S0034-4257(98)00031-5), 1998.
- 968 IPCC: Climate Change 2021 – The Physical Science Basis, Cambridge University Press,
969 <https://doi.org/10.1017/9781009157896>, 2023.
- 970 Jacobson, M. Z.: Strong radiative heating due to the mixing state of black carbon in atmospheric
971 aerosols, *Nature*, 409, 695–697, <https://doi.org/10.1038/35055518>, 2001.
- 972 Jethva, H., Torres, O., and Ahn, C.: Global assessment of OMI aerosol single-scattering albedo
973 using ground-based AERONET inversion, *J. Geophys. Res.*, 119, 9020–9040,
974 <https://doi.org/10.1002/2014JD021672>, 2014.
- 975 Jo, D. S., Park, R. J., Lee, S., Kim, S. W., and Zhang, X.: A global simulation of brown carbon:
976 Implications for photochemistry and direct radiative effect, *Atmos. Chem. Phys.*, 16, 3413–
977 3432, <https://doi.org/10.5194/acp-16-3413-2016>, 2016.
- 978 Junghenn Noyes, K., Kahn, R., Sedlacek, A., Kleinman, L., Limbacher, J., and Li, Z.: Wildfire
979 Smoke Particle Properties and Evolution, from Space-Based Multi-Angle Imaging, *Remote
980 Sens.*, 12, 769, <https://doi.org/10.3390/rs12050769>, 2020a.
- 981 Junghenn Noyes, K. T., Kahn, R. A., Limbacher, J. A., Li, Z., Fenn, M. A., Giles, D. M., Hair, J.
982 W., Katich, J. M., Moore, R. H., Robinson, C. E., Sanchez, K. J., Shingler, T. J., Thornhill,
983 K. L., Wiggins, E. B., and Winstead, E. L.: Wildfire Smoke Particle Properties and Evolution,
984 From Space-Based Multi-Angle Imaging II: The Williams Flats Fire during the FIREX-AQ
985 Campaign, *Remote Sens.*, 12, 3823, <https://doi.org/10.3390/rs12223823>, 2020b.
- 986 Junghenn Noyes, K. T., Kahn, R. A., Limbacher, J. A., and Li, Z.: Canadian and Alaskan wildfire
987 smoke particle properties, their evolution, and controlling factors, from satellite observations,
988 *Atmos. Chem. Phys.*, 22, 10267–10290, <https://doi.org/10.5194/acp-22-10267-2022>, 2022.
- 989 Kahn, R. A., Berkoff, T. A., Brock, C., Chen, G., Ferrare, R. A., Ghan, S., Hansico, T. F., Hegg,
990 D. A., Martins, J. V., McNaughton, C. S., Murphy, D. M., Ogren, J. A., Penner, J. E.,



991 Pilewskie, P., Seinfeld, J. H., and Worsnop, D. R.: SAM-CAAM: A Concept for Acquiring
992 Systematic Aircraft Measurements to Characterize Aerosol Air Masses, *Bull. Am. Meteorol.*
993 *Soc.*, 98, 2215–2228, <https://doi.org/10.1175/BAMS-D-16-0003.1>, 2017.

994 Kahn, R. A., Andrews, E., Brock, C. A., Chin, M., Feingold, G., Gettelman, A., Levy, R. C.,
995 Murphy, D. M., Nenes, A., Pierce, J. R., Popp, T., Redemann, J., Sayer, A. M., da Silva, A.
996 M., Sogacheva, L., and Stier, P.: Reducing Aerosol Forcing Uncertainty by Combining
997 Models With Satellite and Within-The-Atmosphere Observations: A Three-Way Street, *Rev.*
998 *Geophys.*, 61, <https://doi.org/10.1029/2022RG000796>, 2023.

999 Kalashnikova, O. V., Garay, M. J., Bates, K. H., Kenseth, C. M., Kong, W., Cappa, C. D.,
1000 Lyapustin, A. I., Jonsson, H. H., Seidel, F. C., Xu, F., Diner, D. J., and Seinfeld, J. H.:
1001 Photopolarimetric Sensitivity to Black Carbon Content of Wildfire Smoke: Results From the
1002 2016 ImPACT-PM Field Campaign, *J. Geophys. Res. Atmos.*, 123, 5376–5396,
1003 <https://doi.org/10.1029/2017JD028032>, 2018.

1004 Kirchstetter, T. W., Novakov, T., and Hobbs, P. V.: Evidence that the spectral dependence of light
1005 absorption by aerosols is affected by organic carbon, *J. Geophys. Res. D Atmos.*, 109, 1–12,
1006 <https://doi.org/10.1029/2004JD004999>, 2004.

1007 Kleinman, L. I., Sedlacek III, A. J., Adachi, K., Buseck, P. R., Collier, S., Dubey, M. K., Hodshire,
1008 A. L., Lewis, E., Onasch, T. B., Pierce, J. R., Shilling, J., Springston, S. R., Wang, J., Zhang,
1009 Q., Zhou, S., and Yokelson, R. J.: Rapid evolution of aerosol particles and their optical
1010 properties downwind of wildfires in the western US, *Atmos. Chem. Phys.*, 20, 13319–13341,
1011 <https://doi.org/10.5194/acp-20-13319-2020>, 2020.

1012 Laskin, A., Laskin, J., and Nizkorodov, S. A.: Chemistry of Atmospheric Brown Carbon, *Chem.*
1013 *Rev.*, 115, 4335–4382, <https://doi.org/10.1021/cr5006167>, 2015.

1014 Levenberg, K.: A method for the solution of certain non-linear problems in least squares, *Q. Appl.*
1015 *Math.*, 2, 164–168, <https://doi.org/10.1090/qam/10666>, 1944.

1016 Li, L., Dubovik, O., Derimian, Y., Schuster, G. L., Lapyonok, T., Litvinov, P., Ducos, F., Fuertes,
1017 D., Chen, C., Li, Z., Lopatin, A., Torres, B., and Che, H.: Retrieval of aerosol components
1018 directly from satellite and ground-based measurements, *Atmos. Chem. Phys.*, 19, 13409–
1019 13443, <https://doi.org/10.5194/acp-19-13409-2019>, 2019.

1020 Li, L., Che, H., Derimian, Y., Dubovik, O., Schuster, G. L., Chen, C., Li, Q., Wang, Y., Guo, B.,
1021 and Zhang, X.: Retrievals of fine mode light-absorbing carbonaceous aerosols from
1022 POLDER/PARASOL observations over East and South Asia, *Remote Sens. Environ.*, 247,
1023 111913, <https://doi.org/10.1016/j.rse.2020.111913>, 2020.

1024 Li, L., Derimian, Y., Chen, C., Zhang, X., Che, H., Schuster, G. L., Fuertes, D., Litvinov, P.,
1025 Lapyonok, T., Lopatin, A., Matar, C., Ducos, F., Karol, Y., Torres, B., Gui, K., Zheng, Y.,
1026 Liang, Y., Lei, Y., Zhu, J., Zhang, L., Zhong, J., Zhang, X., and Dubovik, O.: Climatology of
1027 aerosol component concentrations derived from multi-angular polarimetric POLDER-3
1028 observations using GRASP algorithm, *Earth Syst. Sci. Data*, 14, 3439–3469,
1029 <https://doi.org/10.5194/essd-14-3439-2022>, 2022.

1030 Liang, Y., Stamatis, C., Fortner, E. C., Wernis, R. A., Van Rooy, P., Majluf, F., Yacovitch, T. I.,
1031 Daube, C., Herndon, S. C., Kreisberg, N. M., Barsanti, K. C., and Goldstein, A. H.: Emissions
1032 of organic compounds from western US wildfires and their near-fire transformations, *Atmos.*
1033 *Chem. Phys.*, 22, 9877–9893, <https://doi.org/10.5194/acp-22-9877-2022>, 2022.

1034 Lim, H.-J. and Turpin, B. J.: Origins of Primary and Secondary Organic Aerosol in Atlanta:
1035 Results of Time-Resolved Measurements during the Atlanta Supersite Experiment, *Environ.*
1036 *Sci. Technol.*, 36, 4489–4496, <https://doi.org/10.1021/es0206487>, 2002.



- 1037 Limbacher, J. A., Kahn, R. A., and Lee, J.: The new MISR research aerosol retrieval algorithm: a
1038 multi-angle, multi-spectral, bounded-variable least squares retrieval of aerosol particle
1039 properties over both land and water, *Atmos. Meas. Tech.*, 15, 6865–6887,
1040 <https://doi.org/10.5194/amt-15-6865-2022>, 2022.
- 1041 Liu, D., He, C., Schwarz, J. P., and Wang, X.: Lifecycle of light-absorbing carbonaceous aerosols
1042 in the atmosphere, *npj Clim. Atmos. Sci.*, 3, 40, [https://doi.org/10.1038/s41612-020-00145-](https://doi.org/10.1038/s41612-020-00145-8)
1043 8, 2020.
- 1044 Liu, Y., Stanturf, J., and Goodrick, S.: Trends in global wildfire potential in a changing climate,
1045 *For. Ecol. Manage.*, 259, 685–697, <https://doi.org/10.1016/j.foreco.2009.09.002>, 2010.
- 1046 Lyapustin, A., Wang, Y., Korkin, S., and Huang, D.: MODIS Collection 6 MAIAC algorithm,
1047 *Atmos. Meas. Tech.*, 11, 5741–5765, <https://doi.org/10.5194/amt-11-5741-2018>, 2018.
- 1048 Lyapustin, A., Wang, Y., Go, S., Choi, M., Korkin, S., Huang, D., Knyazikhin, Y., Blank, K., and
1049 Marshak, A.: Atmospheric Correction of DSCOVR EPIC: Version 2 MAIAC Algorithm,
1050 *Front. Remote Sens.*, 2, 1–10, <https://doi.org/10.3389/frsen.2021.748362>, 2021a.
- 1051 Lyapustin, A., Go, S., Korkin, S., Wang, Y., Torres, O., Jethva, H., and Marshak, A.: Retrievals
1052 of Aerosol Optical Depth and Spectral Absorption From DSCOVR EPIC, *Front. Remote*
1053 *Sens.*, 2, 1–14, <https://doi.org/10.3389/frsen.2021.645794>, 2021b.
- 1054 Markel, V. A.: Introduction to the Maxwell Garnett approximation: tutorial, *J. Opt. Soc. Am. A*,
1055 33, 1244, <https://doi.org/10.1364/josaa.33.001244>, 2016a.
- 1056 Markel, V. A.: Maxwell Garnett approximation (advanced topics): tutorial, *J. Opt. Soc. Am. A*, 33,
1057 2237, <https://doi.org/10.1364/josaa.33.002237>, 2016b.
- 1058 Marquardt, D. W.: An Algorithm for Least-Squares Estimation of Nonlinear Parameters, *J. Soc.*
1059 *Ind. Appl. Math.*, 11, 431–441, <https://doi.org/10.1137/0111030>, 1963.
- 1060 Marshak, A., Herman, J., Szabo, A., Blank, K., Carn, S., Cede, A., Geogdzhayev, I., Huang, D.,
1061 Huang, L. K., Knyazikhin, Y., Kowalewski, M., Krotkov, N., Lyapustin, A., McPeters, R.,
1062 Meyer, K. G., Torres, O., and Yang, Y.: Earth observations from DSCOVR epic instrument,
1063 *Bull. Am. Meteorol. Soc.*, 99, 1829–1850, <https://doi.org/10.1175/BAMS-D-17-0223.1>, 2018.
- 1064 Mok, J., Krotkov, N. A., Arola, A., Torres, O., Jethva, H., Andrade, M., Labow, G., Eck, T. F., Li,
1065 Z., Dickerson, R. R., Stenchikov, G. L., Osipov, S., and Ren, X.: Impacts of brown carbon
1066 from biomass burning on surface UV and ozone photochemistry in the Amazon Basin, *Sci.*
1067 *Rep.*, 6, 1–9, <https://doi.org/10.1038/srep36940>, 2016.
- 1068 Mok, J., Krotkov, N. A., Torres, O., Jethva, H., Li, Z., Kim, J., Koo, J. H., Go, S., Irie, H., Labow,
1069 G., Eck, T. F., Holben, B. N., Herman, J., Loughman, R. P., Spinei, E., Soo Lee, S., Khatri,
1070 P., and Campanelli, M.: Comparisons of spectral aerosol single scattering albedo in Seoul,
1071 South Korea, *Atmos. Meas. Tech.*, 11, 2295–2311, [https://doi.org/10.5194/amt-11-2295-](https://doi.org/10.5194/amt-11-2295-2018)
1072 2018, 2018.
- 1073 Moosmüller, H., Chakrabarty, R. K., and Arnott, W. P.: Aerosol light absorption and its
1074 measurement: A review, *J. Quant. Spectrosc. Radiat. Transf.*, 110, 844–878,
1075 <https://doi.org/10.1016/j.jqsrt.2009.02.035>, 2009.
- 1076 Nanda, S., de Graaf, M., Veefkind, J. P., Sneep, M., ter Linden, M., Sun, J., and Levelt, P. F.: A
1077 first comparison of TROPOMI aerosol layer height (ALH) to CALIOP data, *Atmos. Meas.*
1078 *Tech.*, 13, 3043–3059, <https://doi.org/10.5194/amt-13-3043-2020>, 2020.
- 1079 Pausas, J. G. and Keeley, J. E.: A Burning Story: The Role of Fire in the History of Life, *Bioscience*,
1080 59, 593–601, <https://doi.org/10.1525/bio.2009.59.7.10>, 2009.
- 1081 Petters, M. D., Carrico, C. M., Kreidenweis, S. M., Prenni, A. J., DeMott, P. J., Collett, J. L., and
1082 Moosmüller, H.: Cloud condensation nucleation activity of biomass burning aerosol, *J.*



- 1083 Geophys. Res. Atmos., 114, <https://doi.org/10.1029/2009JD012353>, 2009.
- 1084 Phillips, S. M. and Smith, G. D.: Light Absorption by Charge Transfer Complexes in Brown
1085 Carbon Aerosols, *Environ. Sci. Technol. Lett.*, 1, 382–386, <https://doi.org/10.1021/ez500263j>,
1086 2014.
- 1087 Pokhrel, R. P., Wagner, N. L., Langridge, J. M., Lack, D. A., Jayarathne, T., Stone, E. A.,
1088 Stockwell, C. E., Yokelson, R. J., and Murphy, S. M.: Parameterization of single-scattering
1089 albedo (SSA) and absorption Ångström exponent (AAE) with EC/OC for aerosol emissions
1090 from biomass burning, *Atmos. Chem. Phys.*, 16, 9549–9561, <https://doi.org/10.5194/acp-16-9549-2016>, 2016.
- 1092 Press, W. H., Teukolsky, S. A., Vetterling, W. T., and Flannery, B. P.: Numerical Recipes 3rd
1093 Edition: The Art of Scientific Computing, 3rd ed., Cambridge University Press, USA, 2007.
- 1094 Reid, J. S., Koppmann, R., Eck, T. F., and Eleuterio, D. P.: A review of biomass burning emissions
1095 part II: intensive physical properties of biomass burning particles, *Atmos. Chem. Phys.*, 5,
1096 799–825, <https://doi.org/10.5194/acp-5-799-2005>, 2005a.
- 1097 Reid, J. S., Eck, T. F., Christopher, S. A., Koppmann, R., Dubovik, O., Eleuterio, D. P., Holben,
1098 B. N., Reid, E. A., and Zhang, J.: A review of biomass burning emissions part III: intensive
1099 optical properties of biomass burning particles, *Atmos. Chem. Phys.*, 5, 827–849,
1100 <https://doi.org/10.5194/acp-5-827-2005>, 2005b.
- 1101 Remer, L. A., Davis, A. B., Mattoo, S., Levy, R. C., Kalashnikova, O. V., Coddington, O.,
1102 Chowdhary, J., Knobelspiesse, K., Xu, X., Ahmad, Z., Boss, E., Cairns, B., Dierssen, H. M.,
1103 Diner, D. J., Franz, B., Frouin, R., Gao, B., Ibrahim, A., Martins, J. V., Omar, A. H., Torres,
1104 O., Xu, F., and Zhai, P.-W.: Retrieving Aerosol Characteristics From the PACE Mission, Part
1105 1: Ocean Color Instrument, *Front. Earth Sci.*, 7, 1–20,
1106 <https://doi.org/10.3389/feart.2019.00152>, 2019a.
- 1107 Remer, L. A., Knobelspiesse, K., Zhai, P., Xu, F., Kalashnikova, O. V., Chowdhary, J., Hasekamp,
1108 O., Dubovik, O., Wu, L., Ahmad, Z., Boss, E., Cairns, B., Coddington, O., Davis, A. B.,
1109 Dierssen, H. M., Diner, D. J., Franz, B., Frouin, R., Gao, B., Ibrahim, A., Levy, R. C., Martins,
1110 J. V., Omar, A. H., and Torres, O.: Retrieving Aerosol Characteristics From the PACE
1111 Mission, Part 2: Multi-Angle and Polarimetry, *Front. Environ. Sci.*, 7, 1–21,
1112 <https://doi.org/10.3389/fenvs.2019.00094>, 2019b.
- 1113 Rios, B., Díaz-Esteban, Y., and Raga, G. B.: Smoke emissions from biomass burning in Central
1114 Mexico and their impact on air quality in Mexico City: May 2019 case study, *Sci. Total
1115 Environ.*, 904, 166912, <https://doi.org/10.1016/j.scitotenv.2023.166912>, 2023.
- 1116 Rissler, J., Vestin, A., Swietlicki, E., Fisch, G., Zhou, J., Artaxo, P., and Andreae, M. O.: Size
1117 distribution and hygroscopic properties of aerosol particles from dry-season biomass burning
1118 in Amazonia, *Atmos. Chem. Phys.*, 6, 471–491, <https://doi.org/10.5194/acp-6-471-2006>,
1119 2006.
- 1120 Samset, B. H., Stjern, C. W., Andrews, E., Kahn, R. A., Myhre, G., Schulz, M., and Schuster, G.
1121 L.: Aerosol Absorption: Progress Towards Global and Regional Constraints, *Curr. Clim.
1122 Chang. Reports*, 4, 65–83, <https://doi.org/10.1007/s40641-018-0091-4>, 2018.
- 1123 Sayer, A. M., Hsu, N. C., Eck, T. F., Smirnov, A., and Holben, B. N.: AERONET-based models
1124 of smoke-dominated aerosol near source regions and transported over oceans, and
1125 implications for satellite retrievals of aerosol optical depth, *Atmos. Chem. Phys.*, 14, 11493–
1126 11523, <https://doi.org/10.5194/acp-14-11493-2014>, 2014.
- 1127 Sayer, A. M., Hsu, N. C., Lee, J., Kim, W. V., Burton, S., Fenn, M. A., Ferrare, R. A.,
1128 Kacenelenbogen, M., LeBlanc, S., Pistone, K., Redemann, J., Segal-Rozenhaimer, M.,



- 1129 Shinozuka, Y., and Tsay, S.: Two decades observing smoke above clouds in the south-eastern
1130 Atlantic Ocean: Deep Blue algorithm updates and validation with ORACLES field campaign
1131 data, *Atmos. Meas. Tech.*, 12, 3595–3627, <https://doi.org/10.5194/amt-12-3595-2019>, 2019.
- 1132 Schroeder, W. and Giglio, L.: VIIRS/NPP Thermal Anomalies/Fire Daily L3 Global 1km SIN
1133 Grid V001. distributed by NASA EOSDIS Land Processes DAAC,
1134 doi:10.5067/VIIRS/VNP14A1.001, 2018.
- 1135 Schuster, G. L., Dubovik, O., Holben, B. N., and Clothiaux, E. E.: Inferring black carbon content
1136 and specific absorption from Aerosol Robotic Network (AERONET) aerosol retrievals, *J.*
1137 *Geophys. Res. D Atmos.*, 110, 1–19, <https://doi.org/10.1029/2004JD004548>, 2005.
- 1138 Schuster, G. L., Dubovik, O., and Arola, A.: Remote sensing of soot carbon – Part 1:
1139 Distinguishing different absorbing aerosol species, *Atmos. Chem. Phys.*, 16, 1565–1585,
1140 <https://doi.org/10.5194/acp-16-1565-2016>, 2016.
- 1141 Seiler, W. and Crutzen, P. J.: Estimates of gross and net fluxes of carbon between the biosphere
1142 and the atmosphere from biomass burning, *Clim. Change*, 2, 207–247,
1143 <https://doi.org/10.1007/BF00137988>, 1980.
- 1144 Sengupta, D., Samburova, V., Bhattarai, C., Kirillova, E., Mazzoleni, L., Iaukea-Lum, M., Watts,
1145 A., Moosmüller, H., and Khlystov, A.: Light absorption by polar and non-polar aerosol
1146 compounds from laboratory biomass combustion, *Atmos. Chem. Phys.*, 18, 10849–10867,
1147 <https://doi.org/10.5194/acp-18-10849-2018>, 2018.
- 1148 Sengupta, D., Samburova, V., Bhattarai, C., Watts, A. C., Moosmüller, H., and Khlystov, A. Y.:
1149 Polar semivolatile organic compounds in biomass-burning emissions and their chemical
1150 transformations during aging in an oxidation flow reactor, *Atmos. Chem. Phys.*, 20, 8227–
1151 8250, <https://doi.org/10.5194/acp-20-8227-2020>, 2020.
- 1152 Sinyuk, A., Holben, B. N., Eck, T. F., Giles, D. M., Slutsker, I., Korkin, S., Schafer, J. S., Smirnov,
1153 A., Sorokin, M., and Lyapustin, A.: The AERONET Version 3 aerosol retrieval algorithm,
1154 associated uncertainties and comparisons to Version 2, *Atmos. Meas. Tech.*, 13, 3375–3411,
1155 <https://doi.org/10.5194/amt-13-3375-2020>, 2020.
- 1156 Sinyuk, A., Holben, B. N., Eck, T. F., Giles, D. M., Slutsker, I., Dubovik, O., Schafer, J. S.,
1157 Smirnov, A., and Sorokin, M.: Employing relaxed smoothness constraints on imaginary part
1158 of refractive index in AERONET aerosol retrieval algorithm, *Atmos. Meas. Tech.*, 15, 4135–
1159 4151, <https://doi.org/10.5194/amt-15-4135-2022>, 2022.
- 1160 Sumlin, B. J., Heinson, Y. W., Shetty, N., Pandey, A., Pattison, R. S., Baker, S., Hao, W. M., and
1161 Chakrabarty, R. K.: UV–Vis–IR spectral complex refractive indices and optical properties of
1162 brown carbon aerosol from biomass burning, *J. Quant. Spectrosc. Radiat. Transf.*, 206, 392–
1163 398, <https://doi.org/10.1016/j.jqsrt.2017.12.009>, 2018.
- 1164 Sun, H., Biedermann, L., and Bond, T. C.: Color of brown carbon: A model for ultraviolet and
1165 visible light absorption by organic carbon aerosol, *Geophys. Res. Lett.*, 34, L17813,
1166 <https://doi.org/10.1029/2007GL029797>, 2007.
- 1167 Swap, R. J., Annegarn, H. J., Suttles, J. T., King, M. D., Platnick, S., Privette, J. L., and Scholes,
1168 R. J.: Africa burning: A thematic analysis of the Southern African Regional Science Initiative
1169 (SAFARI 2000), *J. Geophys. Res. Atmos.*, 108, n/a–n/a,
1170 <https://doi.org/10.1029/2003JD003747>, 2003.
- 1171 Torres, O., Bhartia, P. K., Herman, J. R., Ahmad, Z., and Gleason, J.: Derivation of aerosol
1172 properties from satellite measurements of backscattered ultraviolet radiation: Theoretical
1173 basis, *J. Geophys. Res. Atmos.*, 103, 17099–17110, <https://doi.org/10.1029/98JD00900>, 1998.
- 1174 Torres, O., Tanskanen, A., Veihelmann, B., Ahn, C., Braak, R., Bhartia, P. K., Veeffkind, P., and



- 1175 Levelt, P.: Aerosols and surface UV products from Ozone Monitoring Instrument
1176 observations: An overview, *J. Geophys. Res. Atmos.*, 112, 1–14,
1177 <https://doi.org/10.1029/2007JD008809>, 2007.
- 1178 Torres, O., Ahn, C., and Chen, Z.: Improvements to the OMI near-UV aerosol algorithm using A-
1179 train CALIOP and AIRS observations, *Atmos. Meas. Tech.*, 6, 3257–3270,
1180 <https://doi.org/10.5194/amt-6-3257-2013>, 2013.
- 1181 Torres, O., Jethva, H., Ahn, C., Jaross, G., and Loyola, D. G.: TROPOMI aerosol products:
1182 Evaluation and observations of synoptic-scale carbonaceous aerosol plumes during 2018-
1183 2020, *Atmos. Meas. Tech.*, 13, 6789–6806, <https://doi.org/10.5194/amt-13-6789-2020>, 2020.
- 1184 Tritscher, T., Jurányi, Z., Martin, M., Chirico, R., Gysel, M., Heringa, M. F., DeCarlo, P. F., Sierau,
1185 B., Prévôt, A. S. H., Weingartner, E., and Baltensperger, U.: Changes of hygroscopicity and
1186 morphology during ageing of diesel soot, *Environ. Res. Lett.*, 6, 034026,
1187 <https://doi.org/10.1088/1748-9326/6/3/034026>, 2011.
- 1188 Turpin, B. J. and Lim, H.-J.: Species Contributions to PM_{2.5} Mass Concentrations: Revisiting
1189 Common Assumptions for Estimating Organic Mass, *Aerosol Sci. Technol.*, 35, 602–610,
1190 <https://doi.org/10.1080/02786820119445>, 2001.
- 1191 Wang, L., Li, Z., Tian, Q., Ma, Y., Zhang, F., Zhang, Y., Li, D., Li, K., and Li, L.: Estimate of
1192 aerosol absorbing components of black carbon, brown carbon, and dust from ground-based
1193 remote sensing data of sun-sky radiometers, *J. Geophys. Res. Atmos.*, 118, 6534–6543,
1194 <https://doi.org/10.1002/jgrd.50356>, 2013.
- 1195 Wang, X., Sedlacek, A. J., DeSá, S. S., Martin, S. T., Alexander, M. L., Alexander, M. L., Watson,
1196 T. B., Aiken, A. C., Springston, S. R., and Artaxo, P.: Deriving brown carbon from
1197 multiwavelength absorption measurements: Method and application to AERONET and
1198 Aethalometer observations, *Atmos. Chem. Phys.*, 16, 12733–12752,
1199 <https://doi.org/10.5194/acp-16-12733-2016>, 2016.
- 1200 Ward, D. E., Hao, W. M., Susott, R. A., Babbitt, R. E., Shea, R. W., Kauffman, J. B., and Justice,
1201 C. O.: Effect of fuel composition on combustion efficiency and emission factors for African
1202 savanna ecosystems, *J. Geophys. Res. Atmos.*, 101, 23569–23576,
1203 <https://doi.org/10.1029/95JD02595>, 1996.
- 1204 van der Werf, G. R., Randerson, J. T., Giglio, L., Collatz, G. J., Mu, M., Kasibhatla, P. S., Morton,
1205 D. C., DeFries, R. S., Jin, Y., and van Leeuwen, T. T.: Global fire emissions and the
1206 contribution of deforestation, savanna, forest, agricultural, and peat fires (1997–2009), *Atmos.*
1207 *Chem. Phys.*, 10, 11707–11735, <https://doi.org/10.5194/acp-10-11707-2010>, 2010.
- 1208 Wooster, M. J., Roberts, G. J., Giglio, L., Roy, D., Freeborn, P., Boschetti, L., Justice, C., Ichoku,
1209 C., Schroeder, W., Davies, D., Smith, A., Setzer, A., Csizsar, I., Strydom, T., Frost, P., Zhang,
1210 T., Xu, W., de Jong, M., Johnston, J., Ellison, L., Vadrevu, K., McCarty, J., Tanpipat, V.,
1211 Schmidt, C., and San-Miguel, J.: Satellite remote sensing of active fires: History and current
1212 status, applications and future requirements, <https://doi.org/10.1016/j.rse.2021.112694>, 15
1213 December 2021.
- 1214 Xiong, R., Li, J., Zhang, Y., Zhang, L., Jiang, K., Zheng, H., Kong, S., Shen, H., Cheng, H., Shen,
1215 G., and Tao, S.: Global brown carbon emissions from combustion sources, *Environ. Sci.*
1216 *Ecotechnology*, 12, 100201, <https://doi.org/10.1016/j.ese.2022.100201>, 2022.
- 1217 Xu, X., Wang, J., Wang, Y., Zeng, J., Torres, O., Reid, J. S., Miller, S. D., Martins, J. V., and
1218 Remer, L. A.: Detecting layer height of smoke aerosols over vegetated land and water
1219 surfaces via oxygen absorption bands: hourly results from EPIC/DSCOVER in deep space,
1220 *Atmos. Meas. Tech.*, 12, 3269–3288, <https://doi.org/10.5194/amt-12-3269-2019>, 2019.



- 1221 Yu, H., Liu, S. C., and Dickinson, R. E.: Radiative effects of aerosols on the evolution of the
1222 atmospheric boundary layer, *J. Geophys. Res. Atmos.*, 107,
1223 <https://doi.org/10.1029/2001JD000754>, 2002.
- 1224 Zhang, A., Wang, Y., Zhang, Y., Weber, R. J., Song, Y., Ke, Z., and Zou, Y.: Modeling the global
1225 radiative effect of brown carbon: a potentially larger heating source in the tropical free
1226 troposphere than black carbon, *Atmos. Chem. Phys.*, 20, 1901–1920,
1227 <https://doi.org/10.5194/acp-20-1901-2020>, 2020.
- 1228